

Theoretical Studies of α Clustering in Nuclei and Beyond

Takaharu Otsuka^{1,2*}, Alexander Volya³ and Naoyuki Itagaki⁴

^{1*}Department of Physics, University of Tokyo, Hongo 7-3-1, Bunkyo-ku, 1130033, Tokyo, Japan.

²RIKEN Nishina Center for Accelerator-Based Science, Hirosawa 2-1, Wako-shi, 3510198, Saitama, Japan.

³Department of Physics, Florida State University, 311 Keen Building, Tallahassee, 32306-4350, FL, USA.

⁴Department of Physics, Osaka Metropolitan University, 3-3-138 Sugimoto, Osaka, 558-8585, Osaka, Japan.

*Corresponding author(s). E-mail(s): otsuka@phys.s.u-tokyo.ac.jp;
Contributing authors: avolya@fsu.edu; itagaki@omu.ac.jp;

Abstract

This article comprises three sections after an introduction. Section 2 starts with a quick review of the results of *ab initio* no-core shell model calculations by Monte Carlo Shell Model on light nuclei. It is shown that α clustering arises in such first principles calculations for ${}^8, {}^{10}, {}^{12}\text{Be}$ and ${}^{12}\text{C}$ with the Daejeon16 and JISP16 interactions. The α clustering occurs even in well bound states such as the ground state of ${}^{12}\text{C}$. The Hoyle state is shown to be dominated by α clustering in triangular configurations. The crossover between clustering and nuclear matter is demonstrated. As the ground and Hoyle states show strong deformations, they are also good cases to investigate rotational excitations. As an original work, the recently proposed fully quantum (mechanical) formulation for deformation and rotation is extended to cluster or molecular states. Dual rotational modes are proposed: compact-object rotation and distant-object rotation. The former is found in many heavy nuclei, whereas the latter can be found for clustering states in Be and C isotopes. While ${}^8\text{Be}$ is a transparent example for the latter, ${}^{12}\text{C}$ is a rare example that both modes appear in different states of the same nucleus, giving another novel significance to the Hoyle state. The duality of rotation by compact-object and distant-object rotations is a visible outcome of the hierarchy by the cluster formation, placing ${}^{12}\text{C}$ on the border. Atomic molecules and hadrons can be viewed in terms of this duality. Possible relevances to fission is mentioned.

Section 3 presents a general framework for an extended no-core shell model with cluster–nucleon configuration interaction, combining traditional shell-model–like configurations with explicit microscopic configurations representing cluster degrees of freedom. This approach offers a complementary perspective to the strategy discussed in the other sections. The section reviews the microscopic origins of cluster substructures in light nuclei, emphasizing how nucleonic degrees of freedom, nucleon–nucleon interactions, and continuum coupling naturally extend the traditional shell model into configuration–interaction frameworks that incorporate clustering and reaction dynamics. Both methodological developments and applications are discussed, including clustering in well-bound states as well as reaction processes involving alpha clusters.

Section 4 presents that although the cluster structure is robust in Be–C nuclei, some jj -coupling shell model components are mixed with clustering components in the ground state of ^{12}C . This is a different feature than in the cases of the Be isotopes. Using the antisymmetrized quasi cluster model (AQCM), we can clearly model this competition between the cluster and shell components. The spin-orbit interaction is key to realizing the shell structure and contributes more to the ^{12}C case than to the ^8Be case due to closer α – α distances in the former case, thanks to attraction among the clusters.

Keywords: α cluster, Hoyle state, shell model, no-core shell mode, deformation, rotation, triaxiality, dual rotational mode, molecule, fission

1 Introduction

The atomic nucleus consists of Z protons and N neutrons, collectively referred to as nucleons. In the α -clustering picture, illustrated schematically in Fig. 1, the α particle ($Z = N = 2$) (see Fig. 1a) is regarded as a fundamental building block, and certain nuclei may be described as aggregates of α particles, perhaps for main components of some states. In such systems, the condition $Z = N = 2i$ holds, where i is an integer, and the mass number $A = Z + N$ takes the values $A = 4, 8, 12, \dots$. A nucleus is denoted as $^A X$, where X represents the chemical element; for example, ^8Be denotes beryllium–8. Figures 1b–c provide intuitive illustrations of possible α -cluster configurations in ^8Be and ^{12}C , respectively, in which α particles are depicted as mid-sized circles forming a nucleus represented by the surrounding shaded region.

Models based on α clustering have been developed since the 1930s [1–7]. Despite this long history, direct experimental observation of α clustering within nuclei remains challenging. This is partly because α clusters are not fundamental degrees of freedom but rather emergent correlations within an interacting quantum many-body system of nucleons. The Pauli principle and residual nucleon–nucleon correlations may constrain the allowed spatial configurations and/or may lead to substantial mixing between cluster-like and other components in some ways. As a result, geometric cluster pictures provide superb intuition but do not correspond to directly observable structures; instead, experimental signatures of clustering must be inferred indirectly through reaction dynamics and spectroscopic observables. Part of this difficulty also arises from

the intrinsically quantum-mechanical nature of nuclear motion: nuclei are not static objects, and cluster wave functions represent configurations defined in an underlying intrinsic frame rather than in the laboratory coordinate system (see Fig. 1).

Motivated by these challenges, a broad body of theoretical work has been developed, several aspects of which are reviewed in the subsequent sections from different theoretical perspectives. These sections are authored by T. Otsuka, A. Volya, and N. Itagaki, respectively. In particular, a major research project headed by T. Nakamura had been conducted in the recent past years [8] focusing on hierarchy structures involving clustering. A brief comment will be made in relations to Sect. 2.

In Sect. 2, a recent challenge involving super-large-scale *ab initio* no-core shell model calculations for Be and C isotopes is reviewed, depicting the emergence of α (-like) clustering without assuming it *a priori*. Contrary to the usual anticipation that α (-like) clustering appears in the energy region around α -particle emission threshold [5], α (-like) four nucleon correlations, called α clustering for brevity hereafter, emerges even in well-bound states, and its mixing with normal nuclear states lowers the ground-state energy of ^{12}C , for instance. Similar α clustering arises more distinctly in ^8Be and in the Hoyle state of ^{12}C . In other words, nuclear forces and nuclear many-body dynamics favor the α clustering, although details may vary. This work suggests, from first principles viewpoint, that the hierarchy structure with the appearance of the α cluster seems to occur, but may not manifest as clearly as intuitively expected, because of nuclear forces and antisymmetrization constraints. Beyond this review, some new features are discussed. Molecular(-like) configurations of α clusters can naturally result in rotational motion. On the other hand, a new general formulation of rotational bands in atomic nuclei with ellipsoidal shapes has recently been presented [9], where not only the prevailing of triaxial shapes but also the excitation mechanism within a rotational band were major subjects. This new picture can be confronted to the rotational excitation of molecular configurations, and we can indeed analyze their relationship by applying the new formulation. This analysis leads to two basic modes of quantum mechanical rotations. Such study goes beyond the clarification of the α clustering, towards a new unified picture of the rotation of quantum many-body systems, possibly including hadrons and atomic molecules as future applications. All these developments illuminate the importance of the α clustering in the global landscape of physics. The transition between two rotational modes and the hierarchy boundary, likely found in ^{12}C , may show a very interesting coincide [8].

In Sect. 3, α -clustering is reviewed from a microscopic many-body perspective. The section focuses on extended configuration-interaction frameworks that incorporate microscopically constructed cluster configurations, in which full fermionic antisymmetrization and proper treatment of center-of-mass dynamics are maintained. These approaches illustrate how cluster substructures emerge naturally from nucleonic degrees of freedom and realistic nucleon-nucleon interactions. Emphasis is placed on the unified treatment of nuclear structure and reactions, targeting both spectroscopic properties and scattering observables, with representative applications spanning well-bound systems as well as reaction processes involving α clusters.

Sect. 4 provides a complementary review of the competition and coexistence between cluster and shell-model structures in light nuclei. Using the antisymmetrized

quasi-cluster model (AQCM), the section elucidates how α -cluster configurations mix with and can be continuously transformed into jj -coupling shell-model states, thereby offering a unified description of intermediate regimes. Applications to ${}^8\text{Be}$ and ${}^{12}\text{C}$ highlight the decisive role of the spin-orbit interaction in governing cluster persistence and breaking, clarifying the physical mechanisms that drive the evolution from cluster-dominated to shell-model-like structures.

2 First-principle realization of α clustering and dual rotational modes in quantum many-body systems

Quite a few theoretical approaches have been made for the understanding of α clustering in atomic nuclei. Examples such as [11–20] were performed, up to around 2020, including limiting cases like linear chains[3, 19], equilateral triangles[14] and a Bose-Einstein condensate[13]. In about the same and later periods, *ab initio* calculations were reported[21–25]. More references may be mentioned in Sect. 3.

The initial impactful outcome was the appearance of *di- α* clusters in the ground state of ${}^8\text{Be}$ in a VMC calculation [21, 22], similarly to Fig. 1b. The α clustering is more crucial but less clarified for the ${}^{12}\text{C}$ nucleus: this nucleus can be formed by three α particles in configurations, triangular, linear, or others (see Figure 1c). Its lowest spin/parity $J^\pi=0^+$ excited state, the famous Hoyle state[26–28], is a critical gateway in the nucleosynthesis to the present carbon-abundant world filled with living organisms [29, 30], but its structure remains to be clarified. The clarification of these structures lead to a novel picture of dual rotational modes in quantum many-body systems.

2.1 First-principles realization of α clustering in ${}^8\text{Be}$ and ${}^{12}\text{C}$

We now briefly review a set of computational simulations [10] without assuming α clustering *a priori*, which exhibited that α clustering indeed occurs for the ground and excited states of ${}^8,{}^{10},{}^{12}\text{Be}$ and ${}^{12}\text{C}$ isotopes, including the Hoyle state, in varying formation patterns. The simulations are performed by full Configuration Interaction (CI) calculations from first principles with the Daejeon16 interaction [31] for ${}^{12}\text{C}$ and with JISP16 interaction [32] for the Be isotopes, and their validity is further examined for some observables by comparing with experimental data [33] (see [10]). In the

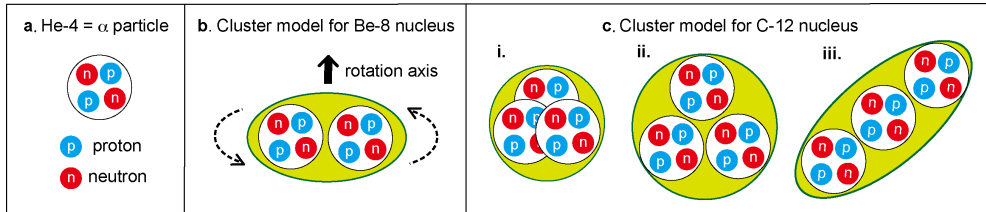


Fig. 1 Schematic illustrations of α clustering in atomic nuclei, for a ${}^4\text{He}=\alpha$ particle, b ${}^8\text{Be}$, and c ${}^{12}\text{C}$ (three possible cases, i, ii and iii). The green areas represent atomic nuclei allowing some movements of α clusters. Taken from [10] with permission.

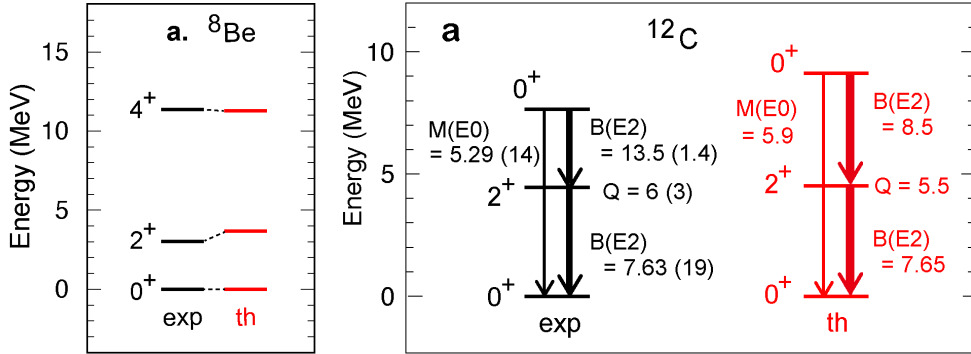


Fig. 2 Level energies of **a** ${}^8\text{Be}$ and **b** ${}^{12}\text{C}$ (left) Experimental data [24, 33], and (right) theoretical results in each panel. Taken from [10] with minor changes with permission.

computational side, the Monte Carlo Shell Model [34–37] has been used for the study of Sect. 2, and relevant results for light nuclei are also shown in [38, 39].

Figure 2a,b display, respectively, the level energies of ${}^8\text{Be}$ and ${}^{12}\text{C}$, both experimental and theoretical, with good experiment-theory agreement. Note that the theoretical calculations were performed in the bound state approximation, which is considered to be sensible for the states to be discussed. We point out that theoretical 0_1^+ and 2_1^+ states can be also obtained up to 99% probability by simply projecting the same intrinsic state ($K^P=0^+$) extracted from the shell model wave functions. Considering large E2 matrix elements related to these states, the 0_1^+ and 2_1^+ states are identified as members of a strongly deformed rotational band with a prolate (an oblate) shape of the deformation parameter $\beta_2 \sim 1$ (0.6) for ${}^8\text{Be}$ (${}^{12}\text{C}$) [10]. This is an important point, and we shall use this feature later. The $B(E2; 2_1^+ \rightarrow 0_1^+)$ value has been also measured experimentally for ${}^{12}\text{C}$ [24] in a high precision, and it has been reproduced well by the present calculation with free charges as displayed in Figure 2b.

The Hoyle state in the theoretical calculation is still too high as compared to the experimental one. This is probably due to the size of the model space (seven harmonic oscillator shells). This model space appears to suffice for the description of the ground and 2_1^+ state, but a somewhat wider space may improve the quality of the description of the Hoyle state. We, however, assume that the present computational setup is sufficient for the discussions below, where conceptual features are main subjects and extrapolations towards better descriptions are also possible.

Figure 3 shows density profiles of the ground, Hoyle and 0_3^+ states of ${}^{12}\text{C}$, and their decompositions according to their structures. The density profile of ${}^4\text{He}$, or α particle, is shown for comparisons. We will later present a beautiful *di- α* structure of ${}^8\text{Be}$ emerging also from first principles. It is mentioned that the present no-core calculation is very suitable for the density profile, because in-medium corrections, including couplings to Giant Resonances, are basically treated explicitly, in contrast to usual shell-model calculations with a one or at most two valence shells.

The α clustering can then be identified by three separate high peaks of the nucleon density, particularly clearly in panels d, e, g, and i. We here decomposed MCSM basis vectors into three groups, (i) medium β_2 (<0.7), (ii) large β_2 (>0.7) not too close to

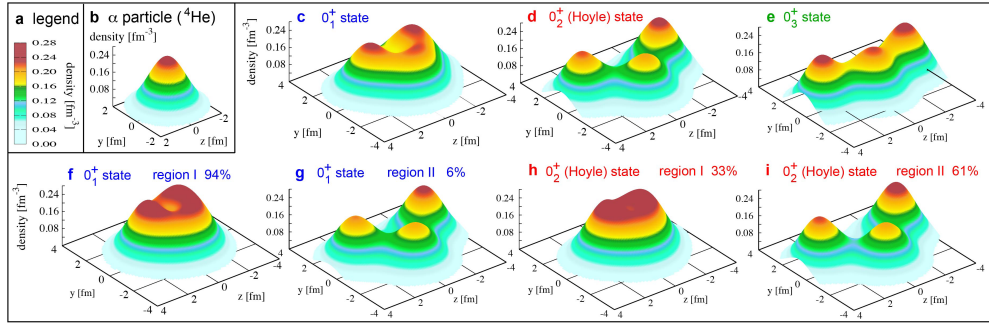


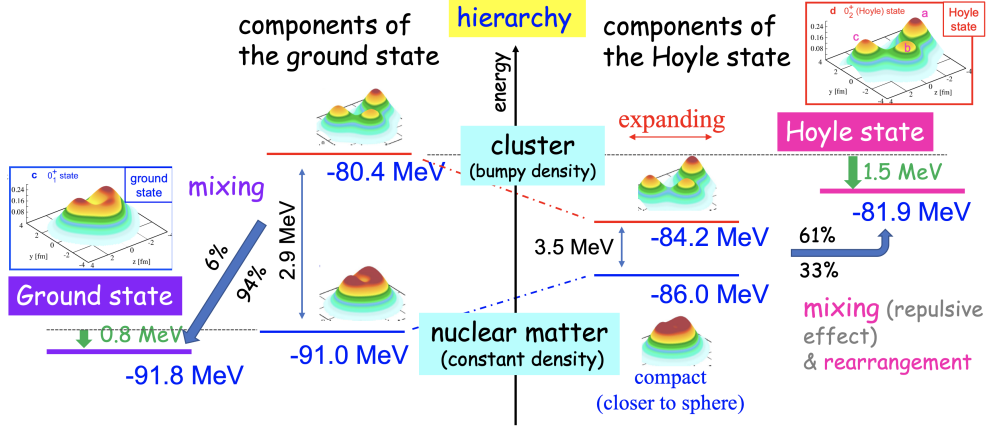
Fig. 3 Density profiles of ^{12}C with that of $^4\text{He}=\alpha$ particle The density profiles for ^{12}C were obtained from intrinsic states, and in panels **i** – **i**, eigenstates are decomposed according to shapes using T-plot analysis. Taken from [10] with permission.

prolate shape ($6^\circ \leq \gamma \leq 60^\circ$), (iii) large β_2 (>0.7) near prolate shape ($\gamma < 6^\circ$). This classification was supported independently by a statistical learning technique in data science [40] (see [10]).

Eigenstates of MCSM calculations are superpositions of these basis vectors. The ground state is composed of group (i) by 94 % (panel **f**), but contains group (ii) by 6 % (panel **g**), which is not negligible. The group (ii) of the ground state (panel **g**) exhibits a clear α clustering. We stress that this occurs in the ground state which is well bound. So, this is not an effect of loose binding, in contrast to some beliefs that α clustering arises as a consequence of weak or no binding near α threshold [5]. In other words, the α clustering can occur without the threshold effect of Ikeda *et al.* [5], but this work does not deny possible appearance of this threshold effect. The α clustering in well-bound states may be one of the very important answer to the α -clustering question from the first principles.

Furthermore, the total density of the Hoyle state (panel **d**) also manifests an even clearer α clustering. As this calculation is still a shell model calculation, all single-particle basis vectors are provided by the eigenfunctions of the harmonic oscillator potential and no explicit continuum components are involved. We still see a good picture of α clustering, probably because the α clustering is also a correlation effect. The above decomposition can be performed for the Hoyle state as well. Panel **h** shows the density profile formed by the basis vectors in group (i), which constitutes 33 % of the eigen wave function. Likewise, Panel **i** shows the density profile by group (ii), which constitutes 61 % of the eigen wave function. A strong mixing is found between a nuclear matter-type density (panel **h**) and a molecular-type density (panel **i**). Because the present 0_2^+ state is formed primarily of the α cluster state and its energy is close to the experimental value of Hoyle state, it is implied that the Hoyle state has thus been reproduced from first principles, apart from possible improvement of the precision. Note that Daejeon 16 interaction was not tuned for this calculation at all.

Thus, α clustering structures emerge from the first principles without assuming them *a priori*, as emphasized in [10]. This can be an important achievement of no-core MCSM calculation powered by Daejeon 16 interaction.



Hierarchy exists, as two modes of the localization due to the force.

The two modes can talk, and can be mixed.

Fig. 4 Overall picture of ground and Hoyle states of ^{12}C

The nuclear-matter-type density profile, characterized by a constant density over a certain region, emerges definitely in the ground state, and rather modestly in the Hoyle states. At the same time, α -clustering-type density profile also emerges in these states, certainly to different extents. It is of interest how building-block states producing these density profiles arise and are mixed. Figure 4 exhibits a sketch for this point.

We begin with the ground state. The two components corresponding to groups (i) and (ii) are located at the energies $E = -91.0$ and -80.4 MeV, as shown in the left half of Fig. 4. Due to the nuclear forces (Daejeon16 interaction in this case), they are mixed, and the resulting state appears at the energy lower by 0.8 MeV, with the mixing probabilities 94% and 6%, respectively, for nuclear matter (group (i)) and cluster (group (ii)) components. Note that the classification was made according to ellipsoidal shapes of basis vector states, but the two components were named after their density-profile characters. The mixing of 6% gives the ground state additional binding energy of 0.8 MeV. Thus, the nuclear forces favor the α clustering even in the middle of nuclear matter, although it may occur mainly around the surface. This surface enhancement is another interesting feature to be further investigated.

We now move on to the Hoyle state. The nuclear-matter component formed by group (i) is located at -86.0 MeV. It is closer to a sphere than the one for the ground state. The cluster component is located at -84.2 MeV, lower by 3.8 MeV than its counterpart for the ground state. This is 7.6 MeV above the ground-state energy, which is closer to the experimental Hoyle-state energy. However, nature is not so nice in this case, and pushes up the mixed state to -81.0 MeV. This repulsive mixing occurs basically because of the orthogonality to the ground state. The mixed state is still below the unperturbed cluster component of the ground state, so there is still some binding-energy gain.

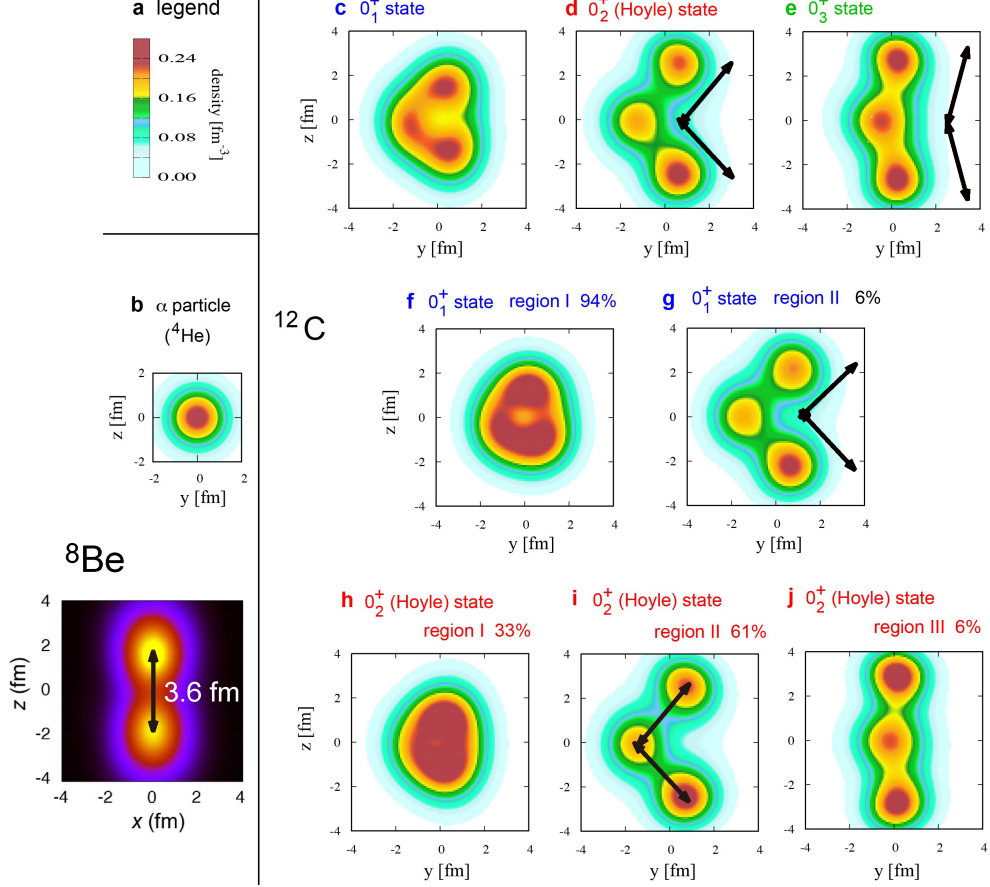


Fig. 5 Two-dimensional representation of matter density profile of ^{12}C compared to ^4He and ^8Be Densities of ^4He and ^8Be are shown in the far left part. Panels **c** - **i** correspond, respectively, to Panels **c** - **i** of Fig. 3. Two-way arrow indicates the distance between two peaks of ^8Be density with the length ~ 3.6 fm, and is also shown for some panels for ^{12}C . Modified from figures in [10] with permissions.

This is a sketch how the ground and Hoyle state are formed. The relation between clustering and normal nuclear matter is considered to be a crossover[41] as pointed out in [10], and appears to be rather complicated as each structure also has variations. Indeed, the mixing between such two structures plays significant roles, especially in the ground state, and may lead us to further understanding of α decay of the states well-bound in general. The cluster-component wave function of the Hoyle state may be somewhat improved by including more single-particle states of harmonic oscillator potential, making individual “clusters” more α -particle-like as a possibility. The positions of those clusters may not substantially change, however. In order to see this point, we show the distances between clusters in Fig. 5. The density profile for ^8Be is shown in the left lower corner of Fig. 5, and the distance between two peaks appears

to be about 3.6 fm. This value is obtained by human eyes, but other manners will lead to similar values. The distance is displayed by two-way arrow. We can put the same arrow with angles tilted in panels for ^{12}C in Fig. 5, where panels **c** - **i** correspond, respectively, to panels **c** - **i** in Fig. 3. We find remarkable similarities between the ^8Be distance and the distances in those ^{12}C cases. The distance ~ 3.6 fm has a special meaning for keeping α -cluster-like structures, as a balance between kinetic energy and binding effects by nuclear forces. For ^{12}C , additional single-particle states of harmonic oscillator potential may shape up wave functions of individual clusters, but may not change their positions much.

Summarizing this subsection, α clustering emerges as a consequence of nuclear forces in the present first principles calculation. The Hoyle state is primarily made up of three α clusters as discussed in quite a few earlier works of various types, but its triangular configuration is presently not equilateral. The ground and 2_1^+ states are members of an oblate rotational band with $\beta_2 \sim 0.6$ [10]. The Hoyle state is also strongly deformed in terms of quadrupole deformation with $\beta_2 \gtrsim 1.0$ [10]. We now turn to discussions on such strongly deformed state and their rotations.

2.2 General description of rotational excitations within quantum many-body theory

In the classical mechanics, a rigid body rotates as sketched in Fig. 6a. This motion evolves as time goes by, following the Newtonian equation.

We then consider the free rotation of a rigid body in the quantum mechanics. The angular momentum has to be quantized. Provided that the rigid body is of axially symmetry, as illustrated in Fig. 6b, the rotational kinetic energy is proportional to $(\vec{J} \cdot \vec{J})$, where the angular momentum of the rigid body is denoted by $\hbar J$. The eigenvalues of the rotational kinetic energy are then proportional to $J(J+1)$.

We now move on to nuclei. In the picture of deformed nuclei proposed by Aage Bohr [42–45], the nucleus is described as a deformed object with a fixed shape filled with a uniform-density matter. It was still a rigid body. The argument in the previous paragraph is applied to the nuclear case. The so-called Bohr Hamiltonian contains a kinetic term representing the rotational motion of this rigid body about three principal axes (see e.g., [46]). By assuming the axial symmetry of this object, the $J(J+1)$ rule of excitation energies within a rotational band arises, exhibiting an account for the origin of observed level-energy regularity ($\propto J(J+1)$) in many nuclei. This axially-symmetric rigid-body picture for deformed nuclei seems to be one of the major elements of the Nobel prize of physics in 1975 [47], and has remained as a paradigm of nuclear rotational bands for (the majority of) the community.

We now turn to another formulation which is free from the classical (or semi-classical) picture/interpretation where a deformed nucleus is regarded as an axially-symmetric rigid-body. In quantum many-body theory, a rotational band can be defined as a set of many-nucleon states, where the member of angular momentum J is generated by projecting a common intrinsic state onto this angular momentum J . This definition itself may not be new, but we start from it and re-formulate the whole description of rotational bands, staying inside quantum mechanics (without resorting

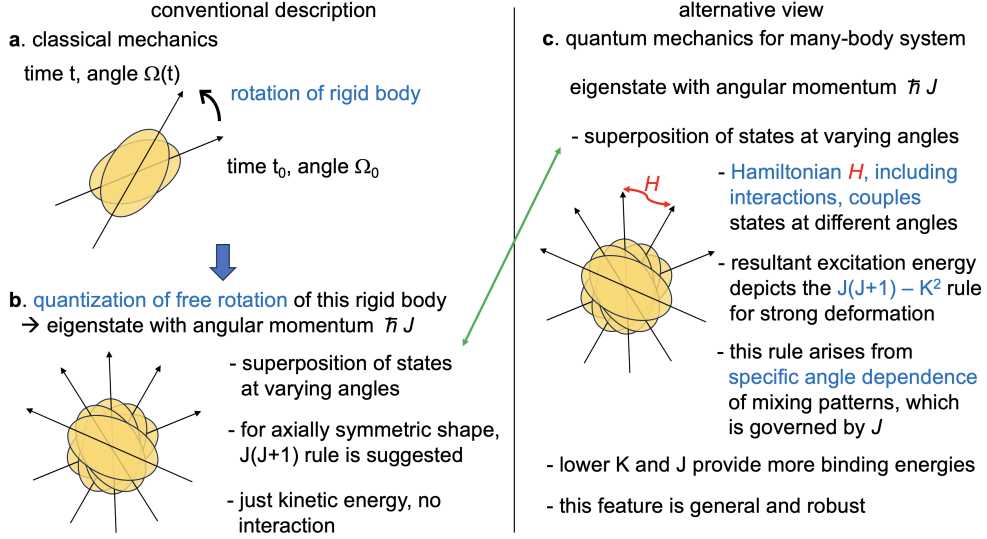


Fig. 6 Schematic illustrations of the rotation in classical and quantum mechanics. a. Classical mechanical view. **b.** Quantization of freely rotating rigid body. **c.** View of the quantum mechanical system composed of many constituents with angular momentum $\hbar J$. The $J(J+1)-K^2$ rule arises. The green arrow indicates similarity in the wave function, but the energy comes from different origins. Taken from Fig. 24 of [9] with kind permission of The European Physical Journal (EPJ).

to the quantization of the free rotation of an axially-symmetric rigid-body). We will come back to differences from conventional formulations later.

We somewhat elaborate on the actual theoretical process as pedagogically as possible, largely because it matters to major discussions later. The angular-momentum projection method is formulated with Wigner's D function (see eq.(9) of [9] where [46] is cited for it), and we begin with its concise sketch. First, the intrinsic state is denoted by ϕ . The state ϕ can be a sophisticated state containing full of correlations by nuclear forces. So, it does not have to be a simple state. From this ϕ , we obtain the state of definite J and M , the total angular momentum and its z-projection in the laboratory frame. This projection can be performed by rotating ϕ in the three-dimensional space with three Euler angles α, β and γ , and by integrating it with an appropriate weighting factor, Wigner's D function. The obtained state is written as,

$$\Psi[\phi, J, M, K] = (2J+1)/(8\pi^2) \int_0^{2\pi} d\alpha \int_0^\pi d\beta \sin\beta \int_0^{2\pi} d\gamma \{D_{M,K}^J(\alpha, \beta, \gamma)\}^* e^{i\alpha\hat{J}_z} e^{i\beta\hat{J}_y} e^{i\gamma\hat{J}_z} |\phi\rangle, \quad (1)$$

where D is the Wigner's function.

Equation (1) implies that the three-fold rotation of ϕ generates states with good (J, M) pairs. One notices an additional index of K . In fact, there can be different and independent states from the same ϕ for a given pair (J, M) , and K specifies them.

By doing the J_z rotation ($e^{i\gamma\hat{J}_z}$) with proper weighting factor, we project ϕ onto a specific value of K , the z -component of \vec{J} of ϕ . In this section, $K=0$ is assumed for clarity, while more general cases can be discussed similarly [9].

This $K=0$ state, denoted by ϕ_0 , is obtained by extracting the relevant parts from eq. (1),

$$\phi_0 = \frac{1}{2\pi} \int_0^{2\pi} d\gamma e^{i\gamma\hat{J}_z} \phi. \quad (2)$$

It is clear that all relevant orientations are superposed with the same amplitude.

We also take $M=0$ without losing generality, because the Hamiltonian is rotationally invariant. The relation

$$D_{M,K}^J(\alpha, \beta, \gamma) = e^{iM\alpha} d_{M,K}^J(\beta) e^{iK\gamma}, \quad (3)$$

is used with $d_{M,K}^J(\beta)$ being the (small) d function. With $M=K=0$, eq. (3) becomes

$$D_{M=0,K=0}^J(\alpha, \beta, \gamma) = d_{0,0}^J(\beta). \quad (4)$$

With this, we consider J -projected norms and Hamiltonian matrix elements. Because of $M=0$, the ϕ_0 state appears for the bra state. The norm of the J -state component contained in ϕ_0 is now given by,

$$\begin{aligned} |\mathcal{N}_J|^2 &= \frac{2J+1}{8\pi^2} \int_0^{2\pi} d\alpha \int_0^\pi d(\cos\beta) \int_0^{2\pi} d\gamma \\ &\quad \langle \phi | \{D_{0,0}^J(\alpha, \beta, \gamma)\}^* e^{i\alpha\hat{J}_z} e^{i\beta\hat{J}_y} e^{i\gamma\hat{J}_z} | \phi \rangle \\ &= \frac{2J+1}{2} \int_0^\pi d(\cos\beta) d_{0,0}^J(\beta) \langle \phi_0 | e^{i\beta\hat{J}_y} | \phi_0 \rangle. \end{aligned} \quad (5)$$

The corresponding quantity for the Hamiltonian, H , is obtained by inserting H after $\langle \phi |$ or $\langle \phi_0 |$.

The normalized expectation value of the Hamiltonian H for the projected state is then given by

$$\begin{aligned} E_J &= \frac{\int_0^\pi d(\cos\beta) d_{0,0}^J(\beta) \langle \phi_0 | H e^{i\beta\hat{J}_y} | \phi_0 \rangle}{\int_0^\pi d(\cos\beta) d_{0,0}^J(\beta) \langle \phi_0 | e^{i\beta\hat{J}_y} | \phi_0 \rangle} \\ &= \frac{\int_0^\pi d(\cos\beta) d_{0,0}^J(\beta) h_y(\beta)}{\int_0^\pi d(\cos\beta) d_{0,0}^J(\beta) n_y(\beta)}, \end{aligned} \quad (6)$$

where the energy and norm kernels are introduced as,

$$h_y(\beta) = \langle \phi_0 | H e^{i\beta\hat{J}_y} | \phi_0 \rangle, \quad (7)$$

and

$$n_y(\beta) = \langle \phi_0 | e^{i\beta\hat{J}_y} | \phi_0 \rangle. \quad (8)$$

The following identity is recalled,

$$d_{0,0}^J(\beta) = P_J(\cos\beta), \quad (9)$$

where $P_J(\cos\beta)$ stands for a Legendre polynomial. By expanding it in terms of $(\cos\beta - 1)^k$, with $k=0, 1, 2, \dots$, the first two terms of the expansion are written as,

$$P_J(\cos\beta) = 1 + J(J+1)/2 (\cos\beta - 1) + \dots \quad (10)$$

The two terms in eq. (10) give a good approximation if $\cos\beta$ is close enough to unity.

The values of $n_y(\beta)$ and $h_y(\beta)$ are reduced quickly as β moves away from 0, as a consequence of strong deformation. With this situation, the d function is approximated as

$$d_{0,0}^J(\beta) = P_J(\cos\beta) \approx 1 + F_J (\cos\beta - 1) \text{ for } \beta \approx 0, \quad (11)$$

with

$$F_J = J(J+1)/2. \quad (12)$$

As the integral is carried out with the variable $\cos\beta$ in eqs. (5) and (6), the d -function in eqs. (5) and (6) is naturally replaced by the function in eq. (11), a polynomial of $(\cos\beta - 1)$.

The range of β runs from 0 to π . Sizable contributions to the quantities are expected also for β close to π , as the overlap is generally restored. For $\beta \sim \pi$, the linear and other approximations starting from $\beta = \pi$ back to smaller values work well also. Although these contributions can be evaluated in the same way as those from $\beta \sim 0$, their concrete description is omitted for brevity.

We define

$$n_k = \int d(\cos\beta) n_y(\beta) (\cos\beta - 1)^k, \text{ for } k = 0, 1, 2, \dots, \quad (13)$$

and

$$e_k = \int d(\cos\beta) h_y(\beta) (\cos\beta - 1)^k, \text{ for } k = 0, 1, 2, \dots. \quad (14)$$

The projected energy of the state of J is given by

$$E_J \approx \frac{e_0 + F_J e_1}{n_0 + F_J n_1}. \quad (15)$$

As the inequalities, $n_1/n_0, e_1/e_0 \ll 1$, hold for strongly deformed states, the energy eigenvalues are then given by,

$$E_J \approx E_0 + J(J+1) \frac{1}{2} \frac{e_0}{n_0} \left\{ \frac{e_1}{e_0} - \frac{n_1}{n_0} \right\}, \text{ with } E_0 = \frac{e_0}{n_0}. \quad (16)$$

The $J(J+1)$ rule of the rotational excitation energy thus emerges within quantum many-body theory for strongly deformed states. We stress that the quantization of free rotation of axially symmetric rigid-body is not used. Some details about the

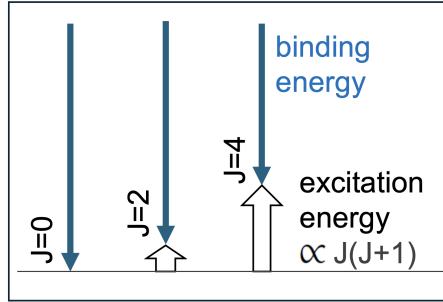


Fig. 7 A graphical illustration of the origin of the $J(J+1)$ rule of excitation energies within a rotational band. Blue downward arrows mean binding energies for the states with the angular momentum $J=0, 2, 4$. The differences from the energy of the $J=0$ state are exhibited by open upward arrows. The present fully quantum mechanical study indicates their height being proportional to $J(J+1)$, if strong ellipsoidal deformation occurs, irrespectively of triaxiality. For $K > 0$, the $\{J(J+1) - K^2\}$ rule is obtained similarly, on top of the $J=K$ state. Taken from figures in [48].

polynomial expansion of the d function are found in [9], including some history. For general $K > 0$ values, more general $\{J(J+1) - K^2\}$ rule has also been given in [9].

The most important property suggested by eq. (16) may be the feature displayed in Fig. 7: the $J(J+1)$ dependence of the excitation energy originates in the J -dependent reduction (i.e., decrease) of the binding energy provided by the Hamiltonian, H . This reduction occurs primarily in the contributions of various parts of the nuclear forces, including single-particle energies, two-nucleon forces, three-nucleon forces, *etc.* All parts give the $J(J+1)$ dependence for strong deformation. In many practical calculations made so far, the kinetic energy appears to be a tiny fraction, or even can work against (lowering rather than raising).

2.3 Rotational excitations built on cluster states

The quantum many-body formulation of the rotational mode presented in the previous subsection can obviously be applied to the ground and 2_1^+ states of ^{12}C , as they are nuclear-matter-type states. The properties shown in Fig. 7 should basically hold for them.

A question arises here as to what picture is appropriate for the states dominated by cluster formation, which differ in structure from nuclear-matter states as discussed in Subsect. 2.1. The most straightforward example may be the ground and 2_1^+ states of ^8Be , where the $di-\alpha$ cluster appears to be a full description of these states as demonstrated in the left lower corner of Fig. 5.

We therefore extend the general formulation described in Subsect. 2.2 so as to be applicable to the case of one cluster, as shown in Fig. 8a, where a small circle stands for a cluster. This is certainly a simplified treatment of more realistic case shown in Fig. 8b, which corresponds to ^8Be case. As the cluster is supposed to be stable internally and have spin zero, its motion as a whole is described in terms of its center of gravity. The intrinsic wave function of this cluster is denoted by ϕ_0 , following the convention of Subsect. 2.2. By definition, it is a $K^P=0^+$ state. We assume that the

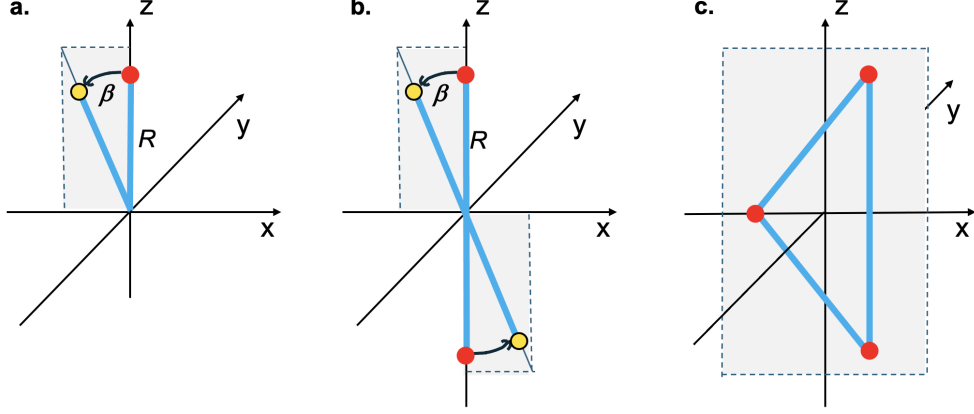


Fig. 8 A schematic illustration of the rotational mode of cluster states.

Red and yellow circles imply clusters for systems with **a** single cluster, **b** two clusters just opposite over the origin, and **c** a possible configuration of three clusters. Yellow circles in **a,b** denote rotation of red ones by angle β in the integral (see the text). In **c**, such rotation angles are too complicated to be included. Gray rectangular boards indicate the planes where clusters are in relevant senses. R stands for the radius of cluster's moving surface. Bold blue lines are to guide the eye.

internal state of the cluster is of angular momentum $J_c=0$ with positive parity, for simplicity.

The overlap between intrinsic state ϕ_0 and its rotated state $e^{i\beta\hat{J}_y}|\phi_0\rangle$ is called norm kernel as mentioned earlier, and is shown in eq. (8). Likewise, the energy kernel is shown in eq. (7). Both quantities should have large magnitudes at and near $\beta=0$, and damp quickly as β moves away from $\beta=0$.

The Hamiltonian H of the present system contains two parts: the kinetic energy of the center of gravity of the cluster, H_g , and the internal part H_i of the cluster. The cluster is considered to be self-contained, implying that the internal state is the lowest eigen state of H_i with the eigenvalue ϵ . We assume this for obtaining the basic picture to start with, and obtain

$$\begin{aligned}
 h_y(\beta) &= \langle \phi_0 | (H_g + H_i) e^{i\beta\hat{J}_y} | \phi_0 \rangle \\
 &= \langle \phi_0 | (H_g + \epsilon) e^{i\beta\hat{J}_y} | \phi_0 \rangle \\
 &= \langle \phi_0 | H_g e^{i\beta\hat{J}_y} | \phi_0 \rangle + \epsilon n_y(\beta).
 \end{aligned} \tag{17}$$

Because the cluster is in the $J_c = 0^+$ ground state with its internal eigen energy denoted by ϵ , the second term on the right-hand-side produces a constant shift of $\epsilon = E_{J_c=0^+}$ (see eq. (6)). Keeping this in mind, we shall not consider contributions of this term hereafter. Likewise, besides H_g and H_i , there is Hamiltonian representing the radial motion of the cluster. It is not considered here either, as the radius of the center of gravity of the cluster is fixed at a given length. This is taken as a reasonable modeling for the present basic picture. Note that various properties of the radial motion, *e.g.*

radial smearing of wave function, can be included in more elaborate calculations at varying levels of sophistication, keeping basic features to be shown here.

In the present case, as shown in Fig. 8b, the center of gravity of the cluster is rotated by the Euler angle β , with a fixed radius, R , from the center of the gravity of the whole nucleus. The center of gravity of the cluster can be treated as a point mass. As the radius is fixed, the relevant part of the Hamiltonian is its zenith-angle dependent part of the kinetic energy, which can be found in any textbook of quantum mechanics:

$$H_g = -\frac{\hbar^2}{2\mathcal{I}} \frac{1}{\sin\beta} \frac{\partial}{\partial\beta} (\sin\beta \frac{\partial}{\partial\beta}), \quad (18)$$

where \mathcal{I} is moment of inertia with $\mathcal{I} = mR^2$ with m being the mass of cluster. The energy kernel is

$$\begin{aligned} h_y(\beta) &= -\frac{\hbar^2}{2\mathcal{I}} \langle \phi_0 | \frac{1}{\sin\beta} \frac{\partial}{\partial\beta} (\sin\beta \frac{\partial}{\partial\beta}) e^{i\beta \hat{J}_y} | \phi_0 \rangle, \\ &= -\frac{\hbar^2}{2\mathcal{I}} \frac{1}{\sin\beta} \frac{\partial}{\partial\beta} (\sin\beta \frac{\partial}{\partial\beta}) n_y(\beta). \end{aligned} \quad (19)$$

By performing partial integration twice, we obtain

$$\begin{aligned} e_0 &= -\frac{\hbar^2}{2\mathcal{I}} \int d\beta \sin\beta \frac{1}{\sin\beta} \frac{\partial}{\partial\beta} (\sin\beta \frac{\partial}{\partial\beta}) n_y(\beta), \\ &= -\frac{\hbar^2}{2\mathcal{I}} [(\sin\beta \frac{\partial}{\partial\beta}) n_y(\beta)]_0^\pi = 0. \end{aligned} \quad (20)$$

Here $(\sin\beta \frac{\partial}{\partial\beta}) n_y(\beta)$ is assumed to vanish at $\beta=0$ and π , as it is very likely.

Similarly, we obtain

$$\begin{aligned} e_1 &= -\frac{\hbar^2}{2\mathcal{I}} \int d\beta (\sin\beta) (\cos\beta - 1) \frac{1}{\sin\beta} \frac{\partial}{\partial\beta} (\sin\beta \frac{\partial}{\partial\beta}) n_y(\beta) \\ &= +\frac{\hbar^2}{2\mathcal{I}} \int d\beta (2 \cos\beta \sin\beta) n_y(\beta), \end{aligned} \quad (21)$$

If $n_y(\beta)$ is non-vanishing only for β very close to 0, this quantity becomes

$$e_1 \approx +\frac{\hbar^2}{2\mathcal{I}} 2 \int d\beta (\sin\beta) n_y(\beta) = +\frac{\hbar^2}{2\mathcal{I}} 2 n_0. \quad (22)$$

Because of eq. (20), $\frac{e_0}{n_0} \frac{n_1}{n_0}$ term in eq. (16) vanishes. Equation (16) then becomes

$$E_J \approx E_0 + J(J+1) \frac{1}{2} \frac{e_1}{n_0} \approx \frac{\hbar^2}{2\mathcal{I}} J(J+1), \quad (23)$$

with

$$E_0 = \frac{e_0}{n_0} = 0. \quad (24)$$

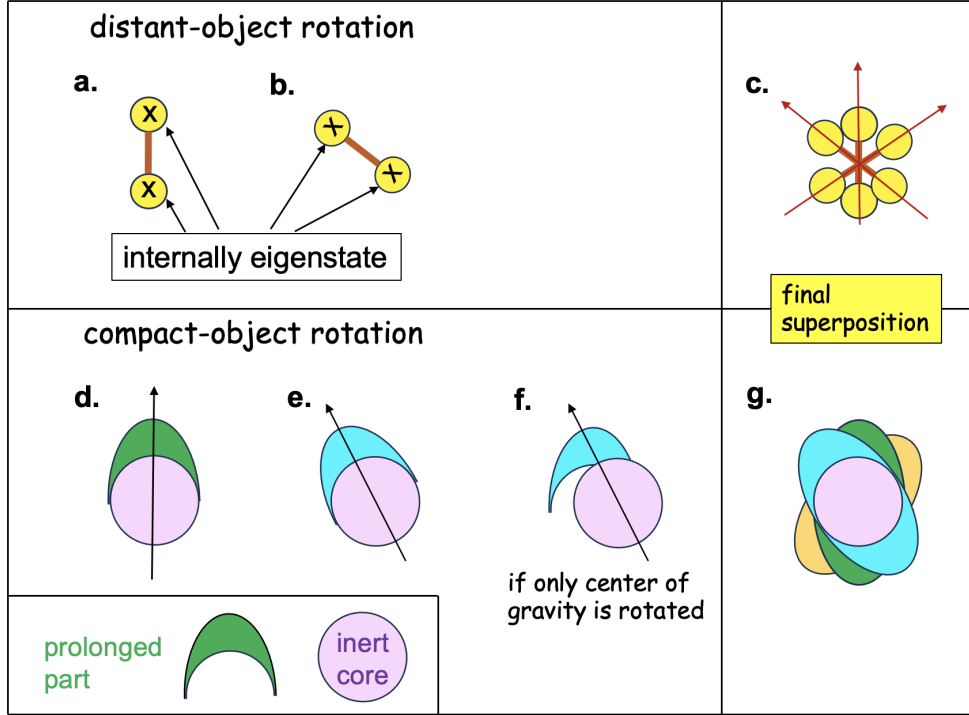


Fig. 9 Conceptual comparison between (upper part) distant-object rotation and (lower part) compact-object rotation. Panels **a** and **b** represent di -cluster system at different orientations, where each cluster is an eigenstate of internal Hamiltonian. Panel **c** schematically displays superposition of the di -cluster system at various orientations, yielding distant-object rotation. Panels **d** and **e** represent the ellipsoid at different orientations. The prolonged parts (green and blue) are coupled by the Hamiltonian including interactions among constituents. Panel **f** shows what would happen if only the center of gravity of blue part were to be rotated to another orientations. Panel **g** schematically displays superposition of the same ellipsoid at various orientations, yielding compact-object rotation.

We thus obtain the energy formula for strongly localized cluster contents. Note that the approximation in eq. (22) does not affect the appearance of the $J(J+1)$ rule, and changes emerge in the coefficient depending on the deviation from this approximation. The deviation is expected to be small for visible clustering cases. The formula looks the same as the equation for the quantized energies of free rotation of a point mass, while corrections to it are also in the scope.

The excitation energy can be similarly derived for di -cluster systems like the one shown in Fig. 8b with proper value of the moment of inertia. Furthermore, the axially symmetric rigid-body follows the same equation. We stress that details of the localization are irrelevant, as n_0 cancel each other between the numerator and the denominator in eq. (23), bringing about a kind of beauty.

It is very interesting that the excitation energy now originates in rotational kinetic energy in contrast to the situation discussed in Subsect. 2.2, the outcome of which is

graphically depicted in Fig. 7. A comparison between these two situations is intuitively illustrated in Fig. 9, where Panels **a-c** exhibit the rotational mode of clustering system and Panels **d-g** are about the rotational mode of ellipsoidal matter system. The “free” rotation of clusters within quantum many-body picture is characterized here: while the wave function of good J is a superposition over all possible orientations, the excitation energy is provided by the total rotational kinetic energy of the centers of gravity of the clusters. Such a natural picture arises from the present formulation.

For the sake of transparency, we now characterize these two types of situations by calling the former “distant-object” rotation (see Figs. 9**a-c**) and the latter “compact-object” rotation (see Figs. 9**d, e** and **g**). Both are quantum mechanical in the sense that the wave functions are superpositions over all orientations with specified amplitudes. However, the dynamical origin differs completely between the two. In the distant-object rotation, each cluster is basically in an eigenstate of its internal Hamiltonian and the excitation energy within a band represents rotational kinetic energy. On the contrary, the compact-object rotation occurs, for instance, with ellipsoids, where the prolonged parts are not eigenstates at all (see Panels **d** and **e**), and those in different orientations are coupled by the Hamiltonian including interactions among constituents, which are nuclear forces presently. The change from Panels **d** to **e** involves proper tilting of the prolonged part. This cannot be made by simply rotating the center of gravity of the prolonged part, as intuitively shown from Panels **d** to **f**. The rotational kinetic term of this center of gravity is considered to yield quite minor contributions because of reduced overlap due to the tilting between Panels **e** and **f**. Note that this overlap remains unity for the distant-object rotation. A classical counterpart probably does not exist for the compact-object rotation.

We note that in both compact-object and distant-object rotations, the $J=0$ state (or state of no spinning) implies that the phase remains the same in all orientations for the same intrinsic state, instead of pointing to one direction.

2.4 Rotational mode in ${}^8\text{Be}$

The formulation of Subsect. 2.3 is applied straightforwardly to the structure of ${}^8\text{Be}$. For simplicity, we identify the peak position of the matter density as the center of gravity of cluster, and the density distribution is assumed to be localized enough, consistently with the picture of Subsect. 2.3. The radius of the center-of-gravity movement is estimated as $R = 1.8$ fm as shown in Fig. 5. From this value, we can obtain

$$E_J \approx 0.80 J(J+1) \text{ MeV}, \quad (25)$$

where J stands for the angular momentum of ${}^8\text{Be}$ nucleus and E_J is the excitation energy of the corresponding state in the rotational band. This gives us $E_{2^+} \approx 4.8$ MeV. This value compares well with the result (≈ 4 MeV) of the *ab initio* no-core MCSM calculation shown in Fig. 2. The moment of inertia parameter should be larger, as the density distribution is somewhat more spread (see Fig. 5). From this viewpoint, the agreement here is considered to be quite good.

The present feature arises from the localization of the cluster (i.e., quick damping of norm kernel), but is independent of details of cluster wave functions, because the

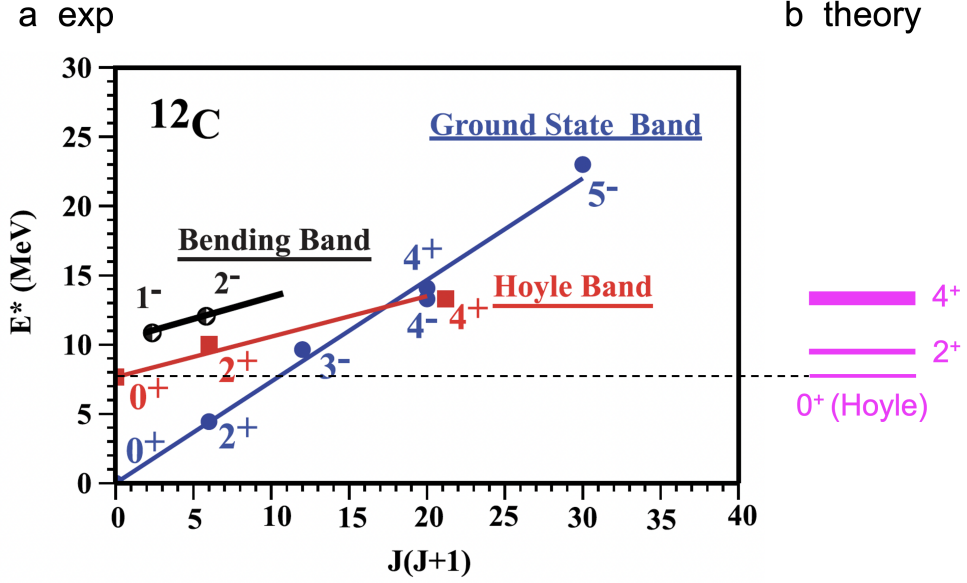


Fig. 10 Possible rotational band built on Hoyle state, **a**, experimental and **b**, theoretical. Panel **a** is taken from [53] with permission. Panel **b** displays the result of the present theoretical estimate with uncertainty depicted by the thickness of the bars due to simple approximation to precise calculation (see text).

same norm kernel appears both in the numerator and the denominator ($\frac{e_1}{n_0}$ in eq. (23)). So, this beautiful feature is robust in this respect.

2.5 Coexistence of two rotational modes in ^{12}C

We now come back to the nucleus ^{12}C , which is not as simple as ^8Be .

The structure of the Hoyle state is of great interests and still attracts attentions of comparatively recent works [49–55]. It is characterized by cluster configurations as suggested in Figs. 3 and 5. For this subsection, the latter figure is more suitable. Figure 5d indicates the emergence of three α -like clusters. We assume that each cluster is rather self-contained and stable, and behaves like an α particle. In fact, by enlarging the single-particle model space in the MCSM calculation, each cluster may better resemble a free α particle. With this expectation, certain properties of the Hoyle state may be described, in a reasonable approximation, as a system of three clusters with individual center of gravity located in the peak positions in Fig. 5d. These positions seem to be useful in further studies, because experimental data of E0 decay [33] and root-mean-square radius [56] compare well with the calculated values [10].

The rotational band built on the ground state has been discussed in Subsects. 2.1 and 2.2. This band is indicated in Fig. 2.

We now discuss another possible rotational band built on the Hoyle state. Its experimental observation has been reported in [52, 53], as displayed in Fig. 10 partly taken

from [53]. Although the establishment of this band may remain open experimentally, we assume it exists in the way proposed. While this band appears above α threshold, we suppose that we discuss doorway states before decays. The Hoyle state and the rotational band are then described by the distant-object rotation of a *tri- α* intrinsic state. However, as depicted in Fig. 5, the *tri- α* configuration is not of axial symmetry, and is indeed triaxial like the one shown in Fig. 8c. The structure is then not as simple as the one for ^8Be .

The intrinsic state, ϕ , represents a *tri- α* state like the one shown in Fig. 8c, putting distortions from the pure (or free) α structure aside. We first look into the K quantum number, which is the z component of the angular momentum. For triaxial configurations like Fig. 8c, three moments of inertia emerge in the classical mechanics, with different values depending on the rotation axis. The moment of inertia about the z axis becomes the smallest. First, we mention that this K value is practically conserved by the same argument as in [9], provided that in ϕ , strong mutual localization of nucleons into small volume of a specified cluster occurs and the center of gravity of each cluster is also localized in the intrinsic state, as expected in the usual α clustering. Certain related details may be found in [57].

Following eq. (14) of [9], the energy of the state with a good K value, denoted by $\Phi[\phi, K]$, is given by

$$h_K = \langle \Phi[\phi, K] | H | \Phi[\phi, K] \rangle \\ \propto \int_0^{2\pi} d\gamma \cos(K\gamma) \langle \phi | H | e^{i\gamma J_z} \phi \rangle. \quad (26)$$

The relevant part of Hamiltonian is the kinetic energy for the rotation about the z axis of the centers of gravity for three α clusters in a fixed configuration, like the one shown in Fig. 8c. The angle of this z -axis rotation is denoted by γ . We then obtain

$$H_\gamma = -\frac{\hbar^2}{2\mathcal{I}} \frac{\partial^2}{\partial \gamma^2}, \quad (27)$$

where \mathcal{I} is the corresponding moment of inertia for this rotation. By performing partial integration twice for eq. (26), h_K is expressed by the product of the norm part and the $\frac{\hbar^2}{2\mathcal{I}} K^2$ term. One then obtains the normalized contribution to the energy,

$$E_K = \frac{\hbar^2}{2\mathcal{I}} K^2. \quad (28)$$

This is nothing but the kinetic rotational energy due to the rotation about the z axis. As this energy increases as K , the lowest state is of $K=0$. It is of interest that $K=0$ is favored both in the distant-object rotation and in the compact-object rotation [9]. In the latter, it is a consequence of the maximization of the binding energy, but in the former it arises in order to avoid rotational kinetic energy with $K > 0$. In fact, by having $K=0$, all orientations about the z axis are superposed with equal amplitudes, and the K^2 expectation value vanishes. This is a quantum realization of “stopped”

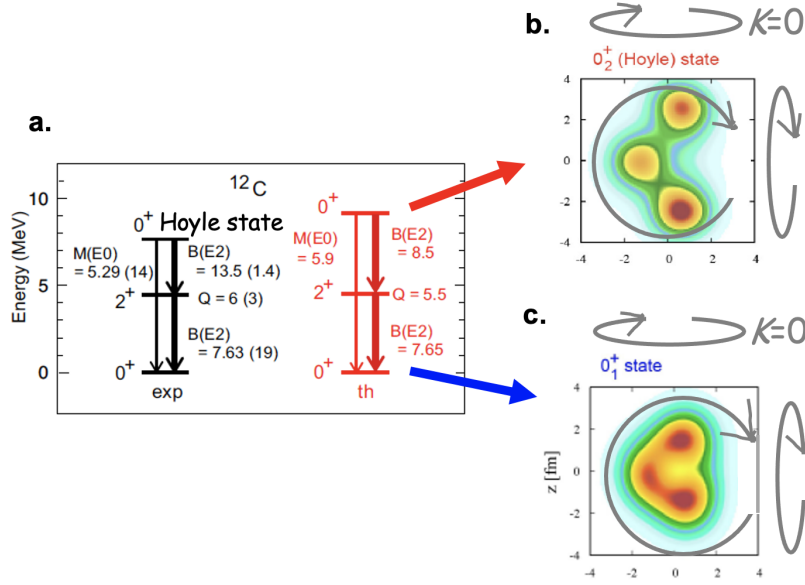


Fig. 11 Schematic picture of proposed rotational bands built on the ground and Hoyle states of ^{12}C . Panel a is taken from [10] with permission. Panels b and c display, respectively, the rotation of the Hoyle and ground states (see text).

(z axis) spinning. It is pointed out that the value of $\mathcal{I}(>0)$ does not matter for the realization of $K=0$ lowest band in the present scheme.

Figure 11 shows how rotational modes are created for the ground and Hoyle states. We start with the Hoyle band. Panel b indicates that the $K=0$ projected intrinsic state enters the process, as discussed above. There are two other axes, x and y (see Fig. 8c). In the classical mechanics, the moment of inertia takes different values for the rotations about these axes. The motion is then considered to be very complicated. In quantum mechanics, the $K=0$ projection comes in, which brings about a kind of averaging over the x -axis and y -axis rotations. This effect can be precisely incorporated by assessing energy kernels following the arguments in Subsect. 2.2 (or eventually [9]), but will be an elaborate work. Anyway, a simple formula like the one $\propto J(J+1)$ arises in the quantum mechanical treatment, if the cluster localization is strong enough.

Putting such an elaborate calculation aside for the time being, we look into physics cases in a simpler manner. We here estimate the moment-of-inertia for the y axis rotation and the x axis rotation in Fig. 8c in a similar approximation used for ^8Be in Subsect. 2.4. For the y -axis rotation axis, the axis perpendicular to the paper plane of Fig. 5 is taken, and the positions of the center of gravity of each cluster are read from the figure. This is precise enough for the present purpose, similarly to the ^8Be case. Fig. 5d is used for this purpose, and the axis goes through the center of gravity of the whole nucleus. The calculated coefficient in front of $J(J+1)$ is about 0.25 MeV. The other value of the moment of inertia is for the x axis rotation, which corresponds to the rotation about the horizontal axis in the paper plane of Fig. 5. This axis goes through

the cluster on the x axis, yielding no contribution from this cluster. The calculated coefficient in front of $J(J + 1)$ is about 0.30 MeV.

The precise calculation can be performed with an appropriate Hamiltonian with a proper $|\phi\rangle$ or $|\Phi[\phi, K]\rangle$. Such calculations are expected to provide results somewhere in between the corresponding values given by the present coefficient equal to 0.25 MeV or 0.30 MeV. This range generates the excitation energies of the 2^+ and 4^+ states in the Hoyle rotational band at 1.50-1.80 MeV and 5.0-6.0 MeV, respectively. The $J(J + 1)$ rule will be maintained well, but other mechanisms like accidental mixing with a nearby state may disturb this regularity. Far right part of Fig. 10 indicates that these values already depict quite interesting agreement with (possible) rotational levels observed in experiments [52, 53].

The ground band presents basically the same property (see Panel c). Because of faster convergence, the energies of the 0_1^+ and 2_1^+ states are calculated precisely enough by the MCSM calculations, which give a proper treatment of the y - and x -axis rotations. Namely, the elaborate calculation was feasible for these states, but infeasible for the Hoyle band due to the current computer resources.

In a comparison to the ^8Be case in Subsect. 2.4, the difference of the observed 2^+ excitation energies between the ^8Be band and the Hoyle band is as large as a factor of three. This agrees, to a good extent, with the present theoretical values: $0.80/0.25=3.2$ and $0.80/0.30=2.67$.

The Hoyle state is of great importance in the nucleosynthesis. The present discussion adds another fundamental significance to it as a showcase of the coexistence of dual rotational modes within the same nucleus: distant-object and compact-object rotations. This is so rare, and further investigations are of extreme importance.

2.6 Summary

In summary, the α -clustering is shown, in First-Principles no-core shell model calculations, to emerge, without assuming it *a priori*, as an effect of nuclear forces. This calculation, performed by the Monte Carlo Shell Model, reproduces various observed quantities. The α -clustering is shown to appear even in the well-bound ground state of ^{12}C , as a non-negligible component. Although, it is not a major component, this mixture lowers the energy of the ground state. In contrast to this, the α -clustering is virtually solo mechanism for the formation of the ^8Be ground state. The α -clustering remains the dominant mechanism for the Hoyle state, where about 2/3 probability of the wave function, with proper superposition of basis vectors, is composed of α -like clustering. There are nuclear-matter components also in the Hoyle state, and it is of interest that the cluster and matter components are mixed repulsively, partly due to the orthogonality to the fully correlated ground state. This is another very interesting point, partly because the ground-state wave function is believed to be almost converged.

The cluster state is deformed, by definition; the density profile is not spherical in its intrinsic structure. As the deformed shape is connected to the rotational excitation, the cluster states are a very good testing ground of the theory of rotational excitations. The recently presented formulation comprising (i) fully quantum-mechanical

derivation of “rotational” excitation energies, (ii) full inclusion of triaxiality as consequences of rotational symmetry and nuclear forces, (iii) practical conservation of K quantum number in contrast to traditional belief, can be applied to clustering states. The same fundamental equation (eq. (16)) is used for the same picture that the intrinsic state pointing to all orientations are superposed properly according to the angular momentum of the state. The difference from the rotational excitation of ellipsoidal matter lies in the relevant parts of the Hamiltonian. For ellipsoidal matter cases, the nucleon-nucleon interactions produce the major contributions to the so-called rotational excitation energy. But, in the case of clustering states, each cluster is basically in eigenstates internally. What matters is the kinetic energy of the center of gravity of each cluster, which can be treated as a point mass. If the relative configuration of these centers of gravity is fixed (allowing quantum fluctuations), the whole system can be described as an intrinsic state to be projected on a given angular momentum (and parity). In this case, the origin of the “rotational” excitation energy is kinetic, and the same fundamental equation gives us the same energy formula as the one obtained from the quantization of free rigid-body with axial symmetry imposed, even for systems without axial symmetry thanks to the K restoration. Rigorously speaking, some of the discussions here may hold only in ideal cases such as perfect α cluster, but such approaches provide us with simple fundamental pictures, from which further understandings of more complicated cases may be developed.

We presented the concept of dual rotational modes: the rotation of nuclear-matter ellipsoid is called compact-object rotation, whereas the rotation of clusters with fixed configuration is called distant-object rotation. We point out that the former occurs, if the range of interactions between constituents (e.g. nucleons for nucleus) and the size of the whole system (e.g. nuclear radius) are comparable. On the other hand, the latter occurs, if the clusters are separated enough and the clusters behave as eigenstates internally. The duality of rotational modes can be interpreted as an outcome of the clustering hierarchy [8], and remains visible despite sizable mixing of two hierarchies, as seen in ^{12}C . It is of great interest to explore, experimentally or theoretically, any physical systems exhibiting these features, including mixed/intermediate situations. In fact, the compact-object rotation is obviously rather special from the global viewpoint of entire physics, and might be one of the treasures of nuclear physics, unrecognized, at least openly, so far. The hadron spectroscopy can be a good candidate, where quark-gluon system can be compact but also can be spread like deuteron or neutron nuggets.

We further add two prospect subsections.

2.7 Prospects 1: Atomic molecules

It is evident that the present formulation extended to distant-object rotation can be applied to atomic molecules [58]. The discussions of ^8Be may be applied to the linearly configured structures of the O_2 and CO_2 molecules, for example. In the O_2 case, by putting O atoms at the red circles in Fig. 8b, the arguments for the ^8Be nucleus can generally be extended to the O_2 molecule.

The structure of the Hoyle state shows certain similarity to the structure of the H_2O molecule; in Fig. 8c, H atoms can be put at the red circles at the top and the

bottom, and O atom at the red circle in the middle. After the $K=0$ projection, the rotational mode can be described with one rotational band on top of the ground state with the moment of inertia with the value between two classical ones obtained for two axes. It is really interesting how we can apply some of the arguments here to molecular structures, while certain approximations will be needed if norm and energy kernels are actually calculated.

2.8 Prospects 2: Fission

The dual rotational modes may have another completely different relevance. That is the nuclear fission [59]. Before fission, the nucleus may be deformed, and shows a compact-object rotation like many other heavy deformed nuclei. In the case of fast neutron capture, the nucleus gains higher values of angular momenta. This angular momentum is conserved. After passing around scission point during the fission process, two fragments are formed, and their mutual rotation likely occurs. This mutual rotation should basically belong to distant-object rotation. For this distant-object rotation, excitation energies must be very low, and states may be quasi-degenerate for a certain period of time, behaving like a linear motion. If the nucleus gains a high value of the angular momentum, this angular momentum is maintained. However, after scission point, the two fragments may start certain distant-object rotations. As this mode has very low excitation energy, the nucleus may decay from its high angular momentum state populated by fast neutron capture to a low-excitation-energy state of similar angular momentum. This means that a sizable energy may be released to neutron emission. This mechanism may facilitate fission process.

On the other hand, individual fission fragments likely generate own rotational modes, which are compact-object rotations with higher excitation energies. The angular momentum of distant-object rotation can be transferred to such compact-object rotations. The interplay between the distant-object rotation and the compact-object rotation may thus occur in certain types of fission with neutron emissions, for instance. As recently explored in [60], the time evolution of the angular-momentum distribution contains exciting open questions, and in such studies, the coupling between two rotational modes can be an interesting aspect.

3 A review on cluster model approaches

3.1 Introduction

One of the enduring challenges of nuclear many-body physics is to elucidate how structures—such as clusters, phonon excitations, and shape changes—emerge from fundamental interactions among nucleons. While considerable progress has been made by describing nuclei in terms of individual protons and neutrons, the phenomenon of nuclear clustering, emergence of cluster degrees of freedom, most notably α -like correlations, and their role in nuclear structure and dynamics remains not fully understood. Indeed, α -particle formation has been suggested since the early days of nuclear science as one of the guiding ideas behind observed decay modes and the unusual stability of certain nuclear configurations [61–63]. Many multi-cluster, molecular-like

states in light nuclei appear near their respective cluster-decay thresholds—a feature succinctly illustrated in the well-known Ikeda diagram [5]—supporting the idea that alpha clusters serve as important building blocks for such states. A version of this diagram is shown in Fig. 12, highlighting the thresholds and pictorially illustrating cluster structures. Explicit α -particle clustering is closely related to pairing and quartet correlations in nuclei [64] and even in randomly interacting quantum many-body systems clusterization seems to naturally emerge [65], the mechanisms behind this remain to be fully explained.

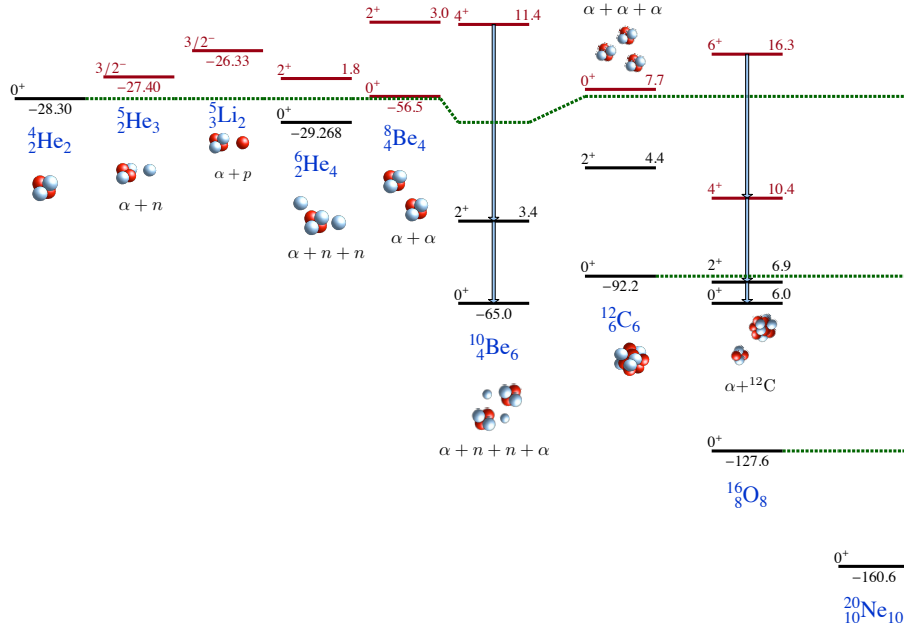


Fig. 12 Ikeda-style diagram illustrating clustering phenomena in light nuclei. The spectra of several light nuclei are shown along with illustrations of their potential clustering structures. Cluster decay thresholds are indicated with dashed lines, and decaying states are highlighted in red. For each state, the spin and parity are shown on the left, and the excitation energy is shown on the right. The total binding energy is indicated for the ground state. All energies are in units of MeV.

Within this paradigm, the connection between the microscopic description of nuclear structure—based on nucleonic degrees of freedom and methods such as the nuclear shell model and, more broadly, configuration interaction—and clustering correlations, preformation, dynamics, and decay remains a central question. Historically, the two descriptions—one based on nucleonic degrees of freedom and the other on cluster degrees of freedom—have largely evolved in parallel. Nevertheless,

the overlap between these parallel lines of thought has been growing. For example, antisymmetrized molecular dynamics has been extensively applied to the study of molecular-type states in clustered nuclei [66], incorporating both clusters and valence nucleons in a molecular-like structure, where valence nucleons mediate bonds between clusters. Present-day advanced models employ fully microscopic descriptions based on nucleon-nucleon interactions and treat cluster dynamics microscopically using methods such as the Resonating Group Method (RGM) [67, 68]. On the other hand, shell model calculations inspired by certain symmetry-based approaches, such as symplectic or $SU(3)$ symmetries, have increasingly been able to capture key aspects of clustering [69–72]. Such symmetry-based methods are among the most promising present-day techniques [73, 74].

Microscopic calculations, such as those using Green’s Function Monte Carlo, have demonstrated the emergence of clustering in ${}^8\text{Be}$ directly from nucleon-nucleon (NN) interactions [21]. This fundamental result has reignited modern, *ab initio*, theoretical interest in clustering. A variety of approaches—including mean-field models [75], lattice simulations [76, 77], large-scale *ab initio* no-core shell model calculations [20], and Bose-Einstein condensate wave studies functions [13, 78, 79]—have been employed to better understand how clusters form and which features of nuclear interactions and many-body dynamics favor the development of correlated substructures. Fully microscopic calculations that integrate nuclear structure and reactions from a configuration interaction perspective have also made significant progress [80–82]. A comprehensive list of references and historical discussions on the subject can be found in review [7].

The study of nuclear clustering is not only about emergent phenomena and the appearance of clustering degrees of freedom; it has become increasingly clear—supported by growing experimental evidence—that clustering plays a fundamental role in connecting nuclear structure and reactions. Clusters are predominantly observed near their corresponding decay thresholds, a pattern first noted by Ikeda [5] and subsequently confirmed by numerous experiments. The physics of open quantum systems have introduced a new perspective in clustering studies [83]. As mentioned earlier, the threshold for a given decay channel significantly impacts the restructuring of the many-body wave function along this channel. This is evident in the observation of cluster states near corresponding thresholds, as well as in the convenient placement of broad states near these thresholds. The effect can manifest in different ways—either enhancing clustering or, conversely, blocking certain decay channels, as seen in proton-decaying ${}^{11}\text{B}$, which inhibits the α -decay pathway [84, 85]. The near-threshold character of clustering makes many of these questions of paramount importance in astrophysics. The astrophysical significance of clustering is epitomized by the Hoyle state in ${}^{12}\text{C}$ [26, 27], whose triple- α nature is crucial for the nucleosynthetic pathway to heavier elements.

Furthermore, recent studies indicate that clustering can persist at high excitation energies and large angular momenta, sometimes in conjunction with rotational phenomena, all while embedded in the continuum of open decay channels [86–90]. This behavior may be driven by superradiance effects, leading to a separation of states into broad, strongly coupled, and structurally organized configurations that facilitate

cluster decay, as well as narrow, trapped states [89]. Recent experimental results leveraging isospin symmetry have highlighted the distinct impact of the continuum on the realignment of wave functions toward clustering [91].

Advances in experimental techniques have significantly expanded the scope of clustering studies. The development of rare isotope beams has enabled novel studies of resonant reactions induced by radioactive nuclei. In particular, the Thick Target Inverse Kinematics (TTIK) approach [92] has proven to be a powerful tool for rare-beam experiments, facilitating the search for α -cluster states and systematic analysis of clustering strength distribution [91, 93–95, 95–100].

Against this backdrop, this chapter reviews how microscopic principles give rise to cluster substructures in light nuclei, with particular emphasis on the essential role of continuum coupling and reaction theory in shaping spectroscopic properties. We approach clustering from the perspective of nucleonic degrees of freedom and nucleon-nucleon interactions, tracing its development from the traditional shell model into configuration interaction techniques that incorporate cluster configurations. This direction occupies a central position, serving as a bridge between various theoretical limits and representing a critical step in the evolution of several related approaches—including algebraic and symmetry-based methods, the resonating group method, the traditional shell model, the no-core shell model, and its continuum extensions.

3.2 Cluster configurations

3.2.1 Center of mass and boosting

As in the standard shell model and no-core shell model approaches, we use the single-particle harmonic oscillator (HO) basis as the foundation of our configuration interaction (CI) framework:

$$\langle \mathbf{r} | n\ell m \rangle = \phi_{n\ell m}(r, \theta, \phi) = \frac{\phi_{n\ell}(r)}{r} Y_{\ell m}(\theta, \phi), \quad (29)$$

where n is the radial quantum number, ℓ the orbital angular momentum, and m its projection. The HO potential is defined by frequency ω , we use m for nucleon mass, the oscillator length $b = \sqrt{\hbar/m\omega}$. The single-particle energy eigenvalues are

$$E = \hbar\omega(N + 3/2), \quad N = 2n + \ell. \quad (30)$$

For explicit expressions and discussion of properties of HO wave functions, see e.g. [101].

Many-body wave functions are expressed as linear combinations of Slater determinants:

$$|\Psi\rangle = \Psi^\dagger|0\rangle = \sum_{\{1, \dots, A\}} \langle 1, \dots, A | \Psi \rangle a_1^\dagger \dots a_A^\dagger |0\rangle, \quad (31)$$

where a_i^\dagger creates a nucleon in a single-particle state labeled by HO quantum numbers and spin. The polymorphism between operators and states allows us to treat Ψ^\dagger as a

many-body creation operator acting on the vacuum. Pauli antisymmetry is ensured by fermionic commutation relations and operator ordering. Products of antisymmetrized states are written as

$$|\mathcal{A}\{\Psi_\alpha\Psi_\beta\}\rangle = \Psi_\alpha^\dagger\Psi_\beta^\dagger|0\rangle. \quad (32)$$

Unlike the traditional shell model, which relies on a predetermined basis, CI methods allow for flexible, on-demand construction of configurations. This generality enables efficient incorporation of physically relevant degrees of freedom, including symmetry-adapted or cluster-like configurations, the construction of those we discuss next.

The center-of-mass (CM) coordinate plays a crucial role in studies of clustering, where identifying and controlling the motion of cluster centers is essential. In traditional shell model calculations, the treatment of the CM has long been recognized as an important issue, particularly in ensuring translational invariance and in interpreting reaction channels. The use of the harmonic oscillator (HO) basis provides a powerful framework for addressing this problem, as it enables exact factorization of the CM degree of freedom due to the rich symmetry structure of many-body HO wave functions.

Following the no-core shell model approach [102], we exploit the symmetry of the many-body HO Hamiltonian, where energy eigenstates are degenerate with respect to the total number of oscillator quanta N . States with fixed N form representations of symmetry groups, including $SU(3)$ and $O(A)$, the latter of which enables exact CM separation in a truncated configuration space defined by a maximum excitation N_{\max} . For states with a given number of quanta

$$N = N_{\text{CM}} + N'. \quad (33)$$

where N_{CM} is the number of quanta in the CM excitation and N' is the number of quanta in the intrinsic wave function. In traditional applications, states of interest are those with $N_{\text{CM}} = 0$, corresponding to a CM in the ground-state oscillator mode:

$$\Psi = \phi_{000}(\mathbf{R})\Psi', \quad (34)$$

where \mathbf{R} is the CM coordinate and Ψ' is the intrinsic wave function [103, 104].

For clustering studies, however, we require more general configurations in which the CM component can take any form. To achieve this, we construct CM-boosted states where the CM motion is expanded in terms of HO eigenfunctions with arbitrary quantum numbers.

$$\Psi_{n\ell m} = \phi_{n\ell m}(\mathbf{R})\Psi', \quad (35)$$

where $N_{\text{CM}} = 2n + \ell$ defines the CM excitation. Although such CM-excited states naturally appear in full shell model diagonalizations—where they are typically regarded as spurious—our approach constructs them directly by acting on the CM coordinate. This CM boost procedure is significantly simpler and requires no additional diagonalization beyond the initial shell model solution [90].

To manipulate the CM motion, we use the standard CM creation and annihilation operators:

$$\mathcal{B}_\mu^\dagger = \frac{1}{\sqrt{2Am\omega\hbar}}(Am\omega R_\mu - iP_\mu), \quad (36)$$

$$\mathcal{B}_\mu = \frac{1}{\sqrt{2Am\omega\hbar}}(Am\omega R_\mu + iP_\mu), \quad (37)$$

which relate to the isoscalar E1 operator:

$$D_\mu = \sqrt{\frac{4\pi}{3}} \sqrt{\frac{\hbar}{2Am\omega}} (\mathcal{B}_\mu^\dagger + \mathcal{B}_\mu). \quad (38)$$

Here, R_μ represents the spherical component μ of the center-of-mass (CM) radius vector, and P_μ is the corresponding component of the CM momentum.

The operator \mathcal{B}_m^\dagger increases N_{CM} by one and transforms as a vector. States with CM in a given state (n, ℓ, m) can be constructed recursively. Node number is increased via the scalar product:

$$\mathcal{B}^\dagger \cdot \mathcal{B}^\dagger = \mathcal{B}_{+1}^\dagger \mathcal{B}_{-1}^\dagger + \mathcal{B}_{-1}^\dagger \mathcal{B}_{+1}^\dagger - \mathcal{B}_0^\dagger \mathcal{B}_0^\dagger, \quad (39)$$

$$\mathcal{B}^\dagger \cdot \mathcal{B}^\dagger \Psi_{n\ell m} = \frac{1}{4} \sqrt{(2n+2)(2n+2\ell+3)} \Psi_{n+1, \ell, m}. \quad (40)$$

Angular momentum ℓ is increased by acting on aligned states:

$$\mathcal{B}_{+1}^\dagger \Psi_{n\ell\ell} = \sqrt{\frac{(\ell+1)(2n+2\ell+3)}{4(2\ell+3)}} \Psi_{n, \ell+1, \ell+1}. \quad (41)$$

The CM angular momentum operator is:

$$\mathcal{L}_\pm = \pm 4\sqrt{2} \left(\mathcal{B}_0^\dagger \mathcal{B}_{\pm 1} - \mathcal{B}_{\pm 1}^\dagger \mathcal{B}_0 \right), \quad (42)$$

with action:

$$\mathcal{L}_\pm \Psi_{n\ell m} = \sqrt{(\ell \mp m)(\ell \pm m + 1)} \Psi_{n\ell, m \pm 1}. \quad (43)$$

The boosted basis (35) generalizes the non-spurious form (34) and preserves translational invariance, as operations on the CM coordinate do not affect the intrinsic structure of Ψ' . A related discussion can be found in Refs. [70, 105, 106].

Next we comment on the structure of CM-boosted states and their connection to SU(3)-based models widely used in the literature [69, 70, 107, 108]. For simplicity, we focus on CM-boosted wave functions of α particles. The ground state of an α particle is dominated by the fully symmetric s^4 configuration, which accounts for more than 90% of the wave function across a wide range of oscillator frequencies $\hbar\omega$. Under the approximation that the α particle has this s^4 structure (equivalent to an $N_{\text{max}} = 0$ truncation), we recover the algebraic limit [69, 70, 108].

In this limit, where the internal excitation is zero ($N' = 0$), the CM-boosted wave function $\Psi_{n\ell m}$ carries all oscillator quanta $N = 2n + \ell$ in the CM motion. The spatial part is fully symmetric under particle exchange, and the SU(3) symmetry of the system is restricted to irreducible representations with $(\lambda, \mu) = (N, 0)$. The wave function can be expanded as:

$$\Psi_{n\ell m} = \sum_{\eta} X_N^{\eta} \Phi_{(N,0):\ell m}^{\eta}, \quad (44)$$

where each term corresponds to a partition $\eta = \{\alpha_i, N_i\}$ satisfying:

$$A = \sum_i \alpha_i, \quad N = \sum_i \alpha_i N_i. \quad (45)$$

Here, A is the total number of nucleons, α_i is the number of particles in oscillator shell i , and N_i the number of quanta associated with that shell.

The expansion coefficients X_N^{η} , known as cluster coefficients [70, 107, 108], are given analytically by:

$$X_N^{\eta} = \sqrt{\frac{1}{4^N} \cdot \frac{N!}{\prod_i (N_i!)^{\alpha_i}} \cdot \frac{A!}{\prod_i \alpha_i!}}. \quad (46)$$

The states $\Phi_{(N,0):\ell m}^{\eta}$ are SU(3)-symmetry states with SU(3) quantum numbers $(\lambda, \mu) = (N, 0)$; such states are unique for each configuration.

This algebraic framework forms the basis of many SU(3)-based shell model studies of α clustering in nuclei [69, 70, 108]. The construction of CM-boosted wave functions via direct CM operations on intrinsic states, as employed in this work, reduces to the SU(3) expansion in the algebraic limit, thereby establishing a direct connection to these earlier models. However, since any intrinsic configuration Ψ' can serve as a starting point, the CM boosting approach is considerably more general applicable to clusters of any size and with realistic internal structure.

One notable limitation of the algebraic framework is the requirement to use the same HO frequency for all nuclei involved—such as the parent, daughter, and α particle in α decay—which can be problematic, as the optimal frequencies for these systems typically differ. While the CM boosting approach retains this frequency-matching constraint, the ability to represent the α particle in a more realistic basis, going beyond the s^4 configuration, helps to alleviate this issue.

In Fig. 13, to highlight the structure of the boosted wave function we illustrate the distribution of nucleons across oscillator shells in a CM-boosted wave function of an s^4 alpha particle, shown for different numbers of center-of-mass (CM) quanta. The structural content of a boosted state is presented in Tab. 1 two illustrative examples of an alpha-particle state boosted by 8 oscillator quanta, denoted as $\Psi_{n=4, \ell=0}^{(\alpha)}$. The left column corresponds to the alpha state described as s^4 ($N_{\max} = 0$) and agrees with the result in (46). The right column shows the case with $N_{\max} = 4$ wave function for the alpha particle calculated using JISP16 nucleon-nucleon interaction Hamiltonian [109] with oscillator basis frequency of $\hbar\omega = 20$ MeV.

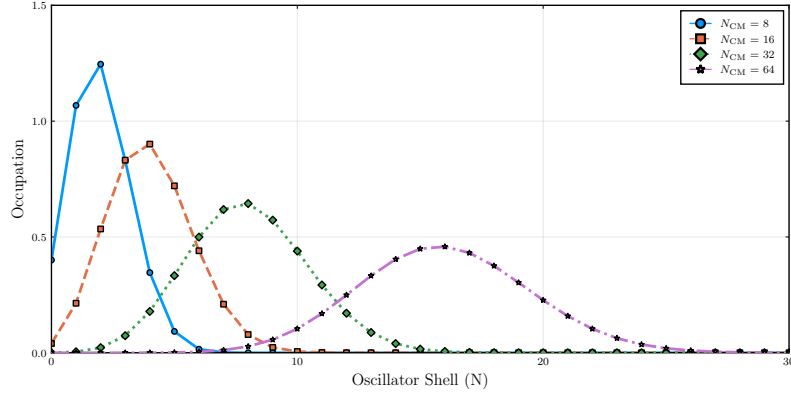


Fig. 13 Nucleonic occupation numbers across oscillator shells in a boosted wave function of an α particle, shown for different values of the center-of-mass (CM) excitation quanta. See ref. [110]

Table 1 Select configuration content of NCSM wave functions for ${}^4\text{He}$ with $\hbar\Omega = 20$ MeV boosted by 8 quanta ($L = 0$). This would correspond to a minimal number of quanta creating an alpha particle configuration within the sd valence space.

Configuration	$N_{\max} = 0$	$N_{\max} = 4$
$(sd)^4$	0.038	0.035
$(p)(sd)^2(pf)^1$	0.308	0.282
$(p)^2(pf)^2$	0.103	0.094
$(p)^2(sd)^1(sdg)^1$	0.154	0.141
$(p)(sd)(sdg)(pfh)^1$	-	0.005
$(p)(sd)(pf)^1(sdg)^1$	-	0.009

3.2.2 Cluster channels

While the formalism is general and allows construction of configurations with multiple clusters it is instructive to concentrate on a two-body problem by considering clusters with A_1 and A_2 nucleons, which combine to form a system of $A = A_1 + A_2$. A *reaction channel* is defined as the asymptotic state of this two-cluster system, composed of wave functions $\Psi^{(1)}$ and $\Psi^{(2)}$ (obtained, for instance, from shell model or NCSM) and their relative motion specified by partial wave ℓ . In line with the standard Resonating Group Method (RGM) or Generator Coordinate Method [67, 68], we construct these channels from center-of-mass (CM) boosted fragments, Eq. (35). We construct the basis states to expand the channel wave functions as follows:

$$\Phi_{nlm} = \mathcal{A} \left\{ \phi_{000}(\mathbf{R}) \phi_{nlm}(\boldsymbol{\rho}) \Psi^{(1)} \Psi^{(2)} \right\}, \quad (47)$$

where \mathcal{A} ensures proper antisymmetrization among all nucleons. In this construction, we recouple the center-of-mass (CM) coordinates of the two clusters into an overall

CM coordinate vector \mathbf{R} and a relative coordinate $\boldsymbol{\rho}$:

$$\mathbf{R} = \frac{A_1 \mathbf{R}_1 + A_2 \mathbf{R}_2}{A_1 + A_2}, \quad \boldsymbol{\rho} = \mathbf{R}_1 - \mathbf{R}_2. \quad (48)$$

To incorporate these channel basis states within the configuration interaction (CI) approach, we focus exclusively on states whose overall CM motion is represented by the ground-state harmonic oscillator (HO) wave function $\phi_{000}(\mathbf{R})$, thus ensuring the states are non-spurious. The relative motion of the two clusters is described by an HO wave function characterized by the chosen quantum numbers n, ℓ, m .

Although expressed in cluster form, Eq. (47) remains a full many-body state that can be represented through Slater determinants (see Eq. (31)). The recoupling of the individual HO wave functions of fragments A_1 and A_2 into combined CM and relative HO wave functions is accomplished using Talmi–Moshinsky–Smirnov coefficients [111]:

$$\Phi_{n\ell}^\dagger = \sum_{n_1 \ell_1, n_2 \ell_2} \mathcal{M}_{n_1 \ell_1 n_2 \ell_2}^{n\ell 00; \ell} \left[\Psi_{n_1 \ell_1}^\dagger \times \Psi_{n_2 \ell_2}^\dagger \right]_\ell. \quad (49)$$

Here we omit the magnetic quantum number m and interpret ℓ as a combined set of asymptotic quantum numbers. The recoupling procedure of constructing a channel basis wave function is illustrated in Fig. 14

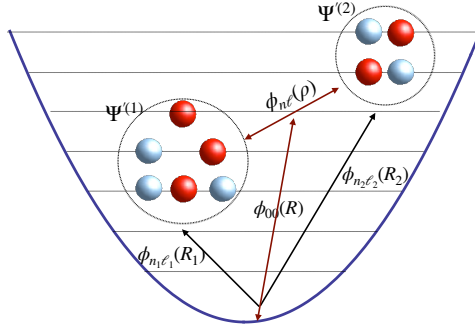


Fig. 14 Illustration showing the construction of the channel basis wave function $\Phi_{n\ell m}$ in (47)

The configurations described in Eq. (47) are obtained directly from existing solutions for the systems A_1 and A_2 and do not require additional diagonalizations. However, these states significantly enlarge the configuration interaction space, making this a powerful cluster-nucleon configuration interaction approach. The variety of available configurations can be further increased by considering channels constructed from excited states of the nuclei. Extensions to multi-cluster systems are also feasible, although analogs of analytic Talmi–Moshinsky coefficients are generally unavailable due to multiple possible recouplings. In such cases, direct construction of channel

states can be accomplished through alternative methods, including algebraic or numerical diagonalization of the relevant Casimir operators associated with the harmonic oscillator algebra.

The full cluster channel is described as a linear combinations of the basis states we defined in (47)

$$|\Xi_\ell\rangle = \sum_n \chi_n |\Phi_{n\ell}\rangle. \quad (50)$$

This effectively expresses the physical relative motion of two fragments (cluster plus core) in harmonic oscillator basis. The amplitudes χ_n are obtained variationally within the Resonating Group Method (RGM) [68, 112], by solving a generalized eigenvalue problem involving Hamiltonian (\mathcal{H}) and norm kernel (\mathcal{N}):

$$\sum_{n'} \mathcal{H}_{nn'} \chi_{n'} = E \sum_{n'} \mathcal{N}_{nn'} \chi_{n'}, \quad \mathcal{H}_{nn'} = \langle \Phi_{n\ell} | H | \Phi_{n'\ell} \rangle, \quad \mathcal{N}_{nn'} = \langle \Phi_{n\ell} | \Phi_{n'\ell} \rangle. \quad (51)$$

Each solution $\{\chi_n\}$ is normalized via

$$\sum_{n,n'} \chi_n^* \mathcal{N}_{nn'} \chi_{n'} = 1. \quad (52)$$

Since the norm kernel \mathcal{N} is positive definite, it admits a unique positive-definite square root. Thus, defining

$$\tilde{\chi}_n \equiv (\sqrt{\mathcal{N}} \chi)_n = \sum_{n'} (\sqrt{\mathcal{N}})_{nn'} \chi_{n'}, \quad (53)$$

we obtain the normalized channel wave function

$$|\tilde{\Xi}_\ell\rangle = \sum_n \tilde{\chi}_n |\Phi_{n\ell}\rangle. \quad (54)$$

Here, absorbing $\sqrt{\mathcal{N}}$ into χ converts Eq. (51) into a standard Hermitian eigenvalue problem. Consequently, the solutions $|\tilde{\Xi}_\ell\rangle$ become orthonormal in the usual sense:

$$\langle \tilde{\Xi}_{\ell'} | \tilde{\Xi}_\ell \rangle = \delta_{\ell'\ell} \quad (55)$$

the orthogonality among different eigenstates similarly follows from the Hermiticity of $\mathcal{N}^{-1/2} \mathcal{H} \mathcal{N}^{-1/2}$.

3.3 Applications

3.3.1 Shell model studies of clustering spectroscopic factors

From the viewpoint of nuclear structure physics the level of clustering in any particular state can be assessed by a spectroscopic factor (SF), defined as the overlap between

cluster channels (50) and shell-model states for a parent nucleus $\Psi^{(A)}$

$$S_\ell \equiv |\langle \Psi^{(A)} | \Xi_\ell \rangle|^2. \quad (56)$$

Since the RGM equations in (51) have in general multiple solutions we can have SF into effectively different channels, which in traditional particle and potential problem would be characterized by a principal quantum number which represents the number of nodes in the wave function.

Historically, many studies of p - and sd -shell nuclei have been carried out within the traditional shell model with a core [69, 71, 107]. Despite its empirical nature, the traditional shell model remains one of the most successful and powerful predictive tools for describing a broad range of nuclear properties [113]. Even in the era of advanced computing and expanding *ab initio* calculations, it continues to play a critical role in bridging fundamental theory and experimental observations. By simplifying the complex nuclear many-body problem, the shell model helps pinpoint and explain a variety of emergent phenomena, including quartet and clustering correlations [64].

Multiple recent studies, fueled by experimental efforts, have been carried out in the mass region bridging the p and sd shells. In particular, advancements in TTIK methods have invigorated this field by systematically investigating clustering above the α -decay threshold [86, 93–95, 95–99, 114]. Recent systematic studies and comparisons with experiment affirm the applicability of the presented approach. However, owing to the inherent limitations of the traditional shell model and its effective nature, many results remain qualitative. In particular, understanding the effective operators involved in four-nucleon (i.e., α -particle) removal requires additional phenomenological adjustments.

Next, we consider several shell-model applications. Let us first focus on low-lying states, where the configuration space is restricted to a single oscillator shell. As a result, the entire cluster spectroscopy is limited to an effective operator within that shell. In an HO basis, this translates to a single $\Phi_{n\ell}$ contributing a non-zero overlap in evaluating the spectroscopic factor:

$$S_\ell \approx |\chi_n|^2 |\langle \Psi^{(A)} | \Phi_{n\ell} \rangle|^2. \quad (57)$$

Within this limit, it is natural to assume all basis states are decoupled, leading to diagonal RGM equations and hence $\chi_n = 1$. Conservation of oscillator quanta enforces this condition, as exploited in analytic studies [115–118].

Figure 15 shows the evaluation of α clustering in $N = Z$, sd -shell nuclei for ground-state-to-ground-state transitions, where $\ell = 0$ and $n = 4$. The dashed black line presents spectroscopic factors calculated via Eq. (57) with $\chi_n = 1$ (labeled as $S^{(\text{old})}$). These values lie an order of magnitude below experimental data and fail to reproduce the observed trend of peaking at the beginning and end of the shell while dipping in the middle. This discrepancy is unsurprising, since an α particle boosted by eight quanta into the sd shell contains only a 4% $(sd)^4$ component, as indicated in Table 1. The issue has prompted significant discussion and highlights the need to renormalize the spectroscopic factors.

A frequently used approach is to adopt the Orthogonality Conditions Model (OCM) spectroscopic factors [107, 119, 120]. Given that the channel wave function's normalization in the limited shell-model space is so small, renormalizing it to unity is a natural choice, thereby establishing a sum rule for the SF in a given channel. Formally, one can argue that the proper RGM solution in an orthonormal basis corresponds to $\tilde{\chi}_n = 1$, and in a diagonal scenario this defines the SM cluster channel as

$$|\Xi_\ell\rangle = \frac{1}{\sqrt{\langle\Phi_{n\ell}|\Phi_{n\ell}\rangle}}|\Phi_{n\ell}\rangle. \quad (58)$$

It is important to emphasize that while Pauli blocking and the projection onto a limited valence space are related, they are distinct reasons for renormalization. Consequently, in OCM the projection onto the valence space is included in the normalization overlap. The spectroscopic factors computed with this renormalization are referred to as $S_\ell^{(\text{ocm})}$ in Fig. 15, and they reproduce both the experimental data and its trend more accurately.

Recent experimental studies [97] have tentatively identified the first limitations of the OCM method, noting that the procedure fails when the normalization due to Pauli blocking becomes extremely small, although further analysis is needed.

3.3.2 Alpha cluster resonances

While some clustered states, such as those in ^8Be , have been known for decades, recent advances in experimental techniques and detailed analyses of scattering spectra have revealed numerous strongly clustered states in many nuclei (see reviews in Refs. [7, 123] and systematic investigations in Refs. [86, 93–95, 95–99, 114]). The strength of clustering is often gauged by comparing the observed α -decay width to the so-called Wigner limit, which represents the maximum possible width for an α particle in a potential model at the experimentally observed energy. Figure 16 illustrates a selection of these strongly clustered states across various light nuclei.

Discussions of α clustering that now includes $N \neq Z$ nuclei, and the influence of valence particles or holes on high-lying cluster states, have been guided by experimental data and theoretical SF evaluations [Eqs. (56) and (58)]. In contrast to older, more restrictive approaches, novel cross-shell effective Hamiltonians now enable significant progress toward a microscopic understanding of clustering in highly excited states and distribution of clustering strength. In particular, the recently developed FSU shell-model Hamiltonian [124, 125], designed for cross-shell particle-hole excitations, has proven invaluable for explaining seemingly excessive experimental clustering strength.

As an example, we highlight the $\ell = 0$ and $\ell = 1$ channels in ^{20}Ne and ^{19}F , which are also included in Fig. 16 as analyzed in Ref. [100]. Selected results appear in Tables 2 and 3, although many other non-clustered states—accurately reproduced by the shell model—are omitted here for brevity. Many additional studies, including those of rotational bands, connection with already mentioned SU(3) symmetry [126] as well as the emergence of rotational bands such as one seen in ^{20}Ne can be found in Ref. [110].

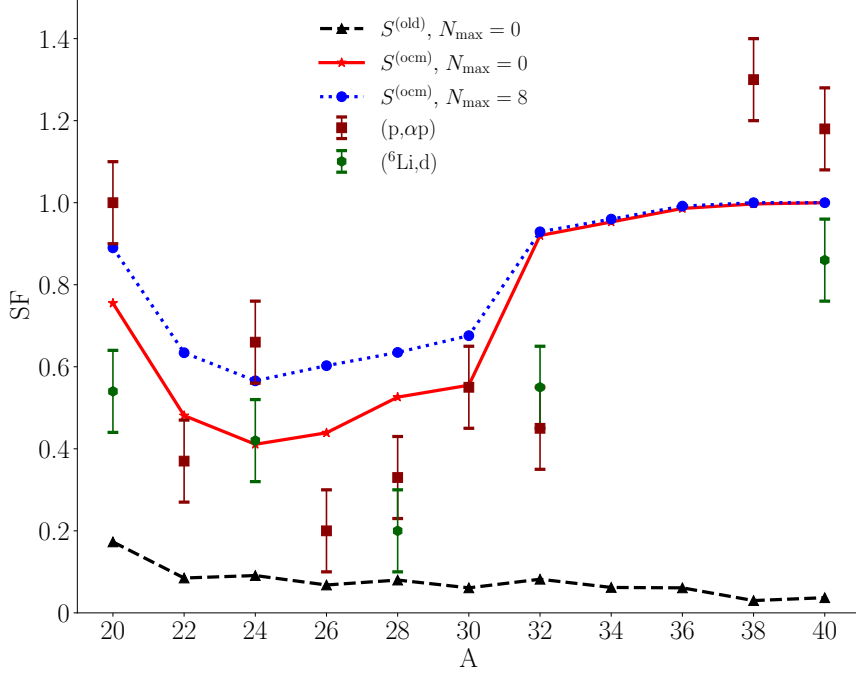


Fig. 15 Spectroscopic factors for ground-state α transitions, $A \rightarrow (A - 4) + \alpha$, in sd -valence $N = Z$ nuclei. Scattered points are experimental data from knockout and pickup reactions [72, 121]. Connected points show theoretical results using the USDB Hamiltonian [122], with the α -particle wave function taken from an NCSM calculation (JISP16, $\hbar\omega = 14$ MeV) at the indicated N_{\max} . The dashed (black) line depicts the traditional shell-model spectroscopic factors [Eq. (57)] with $\chi = 1$, while the solid (red) and dotted (blue) lines show OCM spectroscopic factors. See also ref. [110]

Beyond general theory-experiment comparisons, these studies emphasize the impact of an extra nucleon degree of freedom, as seen by comparing $^{15}\text{N} + \alpha$ and $^{16}\text{O} + \alpha$ decay channels in ^{19}F and ^{20}Ne . In ^{19}F , lower-lying states couple to an $n = 3$ channel that is unavailable in ^{20}Ne due to Pauli blocking; these are low-lying, below-threshold states, and are hence inaccessible to α -scattering experiments. Meanwhile, in the $\ell = 0$ channel, the 6.540 MeV $1/2^-$ state in ^{19}F mirrors the 6.725 MeV 0^+ state in ^{20}Ne , both involving an α particle in an $n = 4$ radial mode. For $\ell = 1$, the 5.79 MeV 1^- resonance in ^{20}Ne couples to the $n = 4$ channel, and higher-lying $n = 4$ clustered states are likewise identified in ^{19}F as the spin-orbit partners $1/2^+$ (5.333 MeV) and $3/2^+$ (5.488 MeV), see Fig. 16.

Although the shell model accurately reproduces many observed features, certain highly excited states remain challenging. For instance, the very broad 0_4^+ state in ^{20}Ne —likely involving an $n = 6$ channel—has a small calculated SF, raising questions about its apparent lack of collectivity in theory. In general, strong clustering appears to emerge from the “collectivization” of cross-shell excitations, in the region of energy where states of a new $\hbar\omega$ structure first appear and exhibit enhanced near-threshold

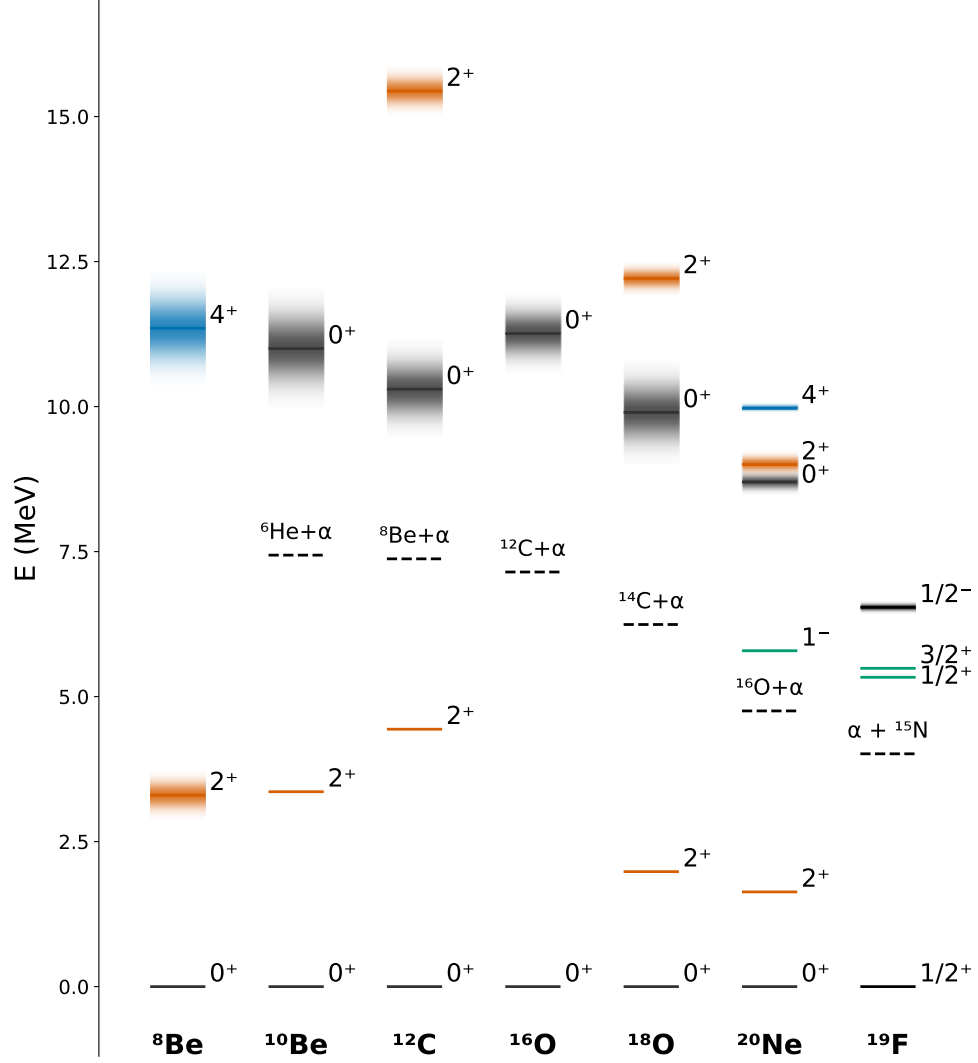


Fig. 16 Selected α -clustered states in several light nuclei, with α -decay thresholds indicated by dashed lines. Above the thresholds the resonances are broadened reflecting their width. The case of ^{20}Ne and ^{19}F , including spin-orbit partners for the $\ell = 1$ channel, is also shown.

strength for each new RGM channel. The mixing across different particle-hole configurations seems to be suppressed in clustered states. However, this phenomenon remains under active investigation. Moreover, the super-radiance effect [89], which seems to drive the collectivization of states deeply embedded in the reaction continuum, has been experimentally observed to play an important role in realigning the wave functions [93, 100].

J_i^π th	$E(\text{MeV})$ th	n th	SF_α th	$E(\text{MeV})$ exp	γ_α exp
0_1^+	0	4	0.755	0	
0_2^+	6.698	4	0.143	6.725	0.47
0_3^+	7.547	5	0.007	7.191	0.017
0_4^+	10.121	6	0	8.7	broad
0_8^+	13.521	5	0.246		
1_1^-	6.982	4	0.381	5.79	1.4
1_2^-	7.918	4	0.379	8.708	

Table 2 Lowest states coupled to $\ell = 0$ and $\ell = 1$ clustering channels in ^{20}Ne for the $^{16}\text{O}+\alpha$ Columns identify state, theoretical excitation energy, number of nodes in the alpha channel, experimental energy, experimental alpha reduced width. The labels in the second row “th” or “exp” refer to results coming from theory and experiment, respectively. Correspondence between data from theory and experiment represent a suggested assignment. The data is from ref. [100]

J_i^π th	$E(\text{MeV})$ th	n th	SF_α th	$E(\text{MeV})$ exp	γ_α exp
$1/2_1^-$	0.468	4	0.706	0.110	
$1/2_2^-$	6.900	4	0.020	(6.095)	
$1/2_3^-$	7.092	4	0.041	7.048	0.12
$1/2_5^-$	7.856	4	0.101	6.540*	0.53
$1/2_1^+$	0.000	3	0.874	0.000	
$1/2_2^+$	6.060	4	0.311	5.333*	1.16
$3/2_1^+$	1.770	3	0.672	1.554	
$3/2_4^+$	6.937	4	0.633	5.488*	0.98

Table 3 Lowest $\ell = 0$ and $\ell = 1$ states in ^{19}F , viewed as $^{15}\text{N}+\alpha$ channels. Columns are analogous to Table 2.

3.3.3 Cluster Nucleon Configuraiton Interaction

Going beyond the analysis of spectroscopic factors discussed in the previous subsections, we next apply the Cluster Nucleon Configuration Interaction (CNCIM) approach to ^{21}Ne as a simple illustration, demonstrating that a drastically reduced channel basis can still reproduce key features of a full shell-model (SM) calculation. This offers a powerful extension to the traditional shell model, especially in cases where full diagonalization is not feasible. We treat ^{20}Ne as a ^{16}O core plus α system, then add a neutron in the $d_{5/2}$ orbital. Concretely, we place an α particle with relative angular momentum $L = 0, 2, 4, 6$ onto ^{16}O and couple with the extra neutron, yielding 18 channel basis states—compared with 1935 many-body states in the full sd SM space.

In this reduced, non-orthogonal basis, we compute the Hamiltonian kernel using the USDB interaction [122] and solve it via the Resonating Group Method (RGM). Figure 17 shows the resulting low-lying spectrum, alongside the full USDB calculation and experimental data. Ground states indicate total binding; energies of other levels are shown relative to the ground state. The main spectral features and excitation

energies are well reproduced, although we note that simple RGM model underbinds by about 3.5 MeV compared to the full diagonalization.

Figure 17 also includes a first column that lists the diagonal energies of the RGM basis states, $\langle \Xi_{JL} | H | \Xi_{JL} \rangle$, where total angular momentum J couples L with the unpaired neutron ($j = 5/2$). The RGM solution clarifies the mixing of partial waves; for example, two $5/2^+$ states with $L = 0$ and $L = 4$ at 1.04 and 2.89 MeV in the first column undergo two-state mixing and repel each other. This implies that the first excited $5/2^+$ state in ^{21}Ne is a mixture of $L = 0$ and $L = 4$, excluding $L = 2$ —a fact confirmed experimentally [127]. Further details of this study including matrix elements of the Hamiltonian and the norm kernel can be found in [106]

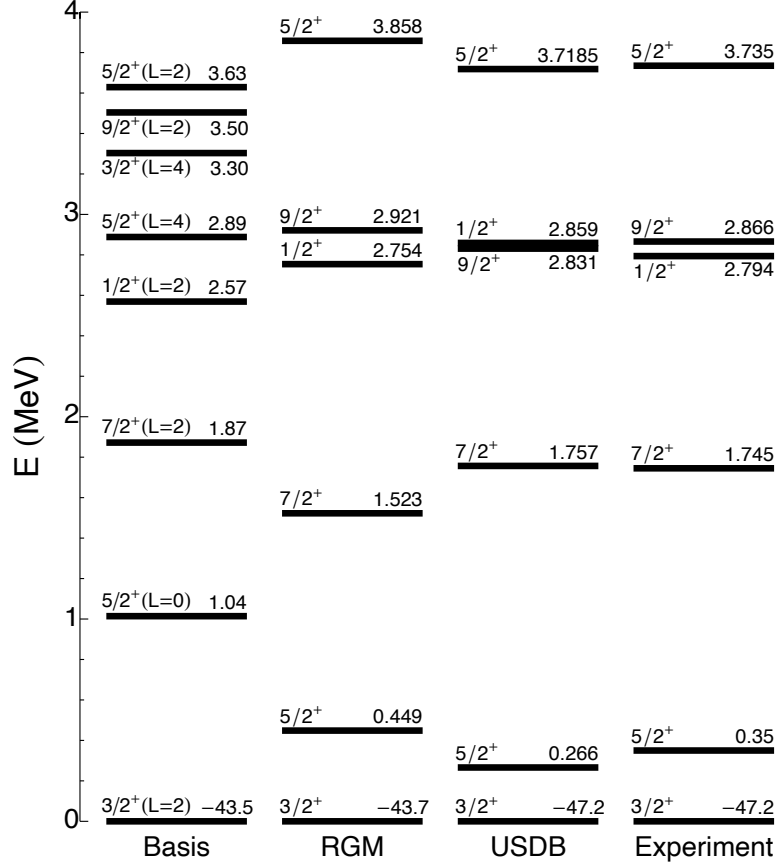


Fig. 17 Diagonal energies in the channel basis, low-lying states in RGM solution, full USDB and experimental spectra of ^{21}Ne , see Ref. [110]

3.3.4 Cluster relative motion

Next, we move our discussion to clustering aspects in *ab initio* no-core applications of shell-model (SM) methods. We begin with the nucleus ${}^8\text{Be}$, which, with its $\alpha + \alpha$ structure, has long served as a benchmark for nuclear clustering studies [21, 77, 108, 128–131].

Table 4 presents both experimental and theoretical energies/widths for the 0^+ , 2^+ , and 4^+ cluster resonances, each interpreted as two α particles with relative angular momenta $\ell = 0, 2, 4$. A treatment based on the Resonating Group Method (RGM), which effectively employs a cluster-configuration-interaction (CI) approach with up to 12 basis channel states, in contrast to a full many-body expansion that would be prohibitively large. Here JISP16 [109] interaction with $\hbar\omega = 25$ MeV is used.

A key signature of rotational two-alpha dynamics is the ratio R_{42} of 4^+ to 2^+ excitation energies, which is found to be about 3.5—close to the $R_{42} = 3.3$ expected from a rotational band. Figure 18 shows the radial wave function for the 0^+ channel,

$$u_\ell(\rho) = \sum_n \chi_n \phi_{n\ell}(\rho), \quad (59)$$

illustrating the effect of different harmonic-oscillator parameters $\hbar\omega$. Beyond the spatial size of each α cluster, $u_\ell(\rho)$ describes the relative motion of the two α particles and can be matched to external Coulomb wave functions allowing to study asymptotic normalization and decay widths.

The decay widths in Table 4 are extracted using the standard R -matrix approach [132],

$$\Gamma_\ell = \frac{\hbar^2 k}{\mu} \frac{\rho_c^2 u_\ell^2(\rho_c)}{F_\ell^2(\eta, k\rho_c) + G_\ell^2(\eta, k\rho_c)}, \quad (60)$$

by matching the interior wave function to the asymptotic solution at $\rho_c = 3.6$ fm. Beyond the range of the nuclear potential, the result is not sensitive to the exact matching point; however, in a restricted HO basis, this issue must be treated with care. The chosen matching location maximizes the outgoing flux while minimizing sensitivity to the matching point. This study simultaneously reproduces the nearly-bound 0^+ ground state ($\Gamma = 5.6$ eV) and the broad 4^+ resonance, highlighting the effectiveness of the cluster-based RGM approach.

ℓ	E_{ex}	Γ	$E_{\text{ex}}^{(\text{RGM})}$	$\Gamma^{(\text{RGM})}$	S_ℓ
0	0.0	5.6*	0.0	8.9*	0.69
2	3.0	1.5	4.6	1.4	0.66
4	11.4	3.5	16.0	2.7	0.51

Table 4 Experimental and RGM results for ${}^8\text{Be}$ with the JISP16 interaction, allowing up to 12 HO quanta in each ℓ channel. Energies and widths are given in MeV except for those marked with * (in eV).

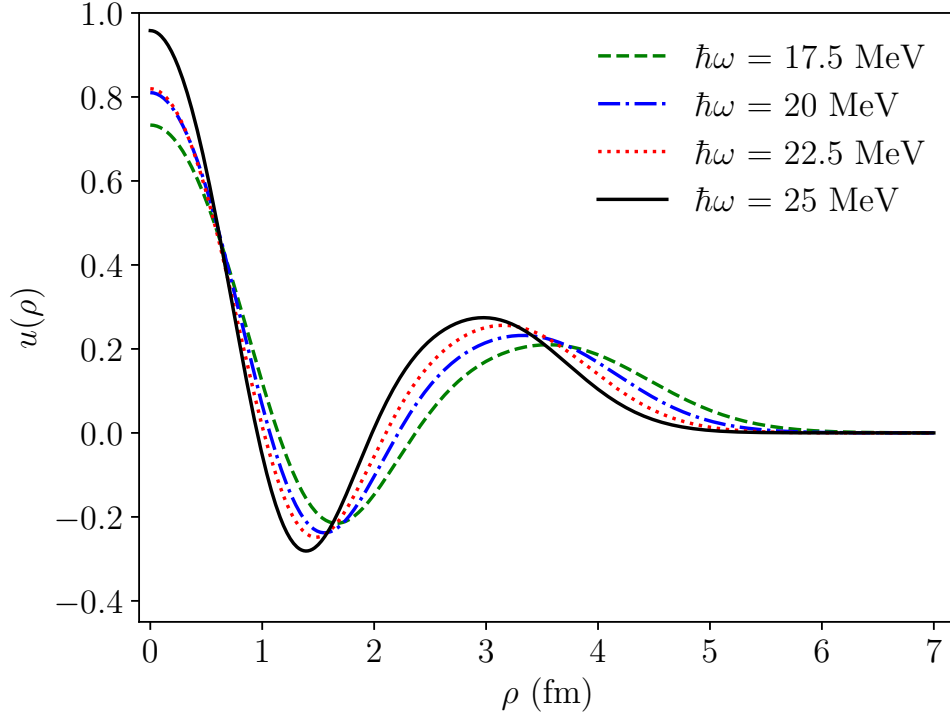


Fig. 18 Relative $\alpha + \alpha$ wave function for the 0^+ RGM channel in ${}^8\text{Be}$, computed using the JISP16 interaction. Different curves correspond to various values of $\hbar\omega$.

3.3.5 Hoyle state

One important future direction of the method is its extension to multi-cluster problems. A classic example is the Hoyle state in ${}^{12}\text{C}$, which has been studied in various approaches [14, 76, 133]. The Hoyle state, an excited 0^+ state just 285 keV above the triple-alpha threshold, decays almost exclusively via an intermediate ${}^8\text{Be}$ resonance, itself only 93 keV above the two-alpha threshold [134–137]. This sequential decay path, in addition to being favored by Coulomb dynamics, highlights important structural features of the three-alpha configuration. A first application of the method to this problem is presented in Ref. [110], and we summarize it below.

While no direct analytic method analogous to Moshinsky coefficients exists for the three-cluster case, the channels can be constructed through a sequential coupling of Jacobi coordinates. In the present calculation, up to $N_{\text{max}} = 12$ oscillator quanta are distributed among the two relative coordinates. The RGM framework is applied to a system of three identical α particles, each in an s^4 configuration, using the JISP16 interaction with $\hbar\omega = 25$ MeV. The minimal configuration allowed by the Pauli principle corresponds to $N = 8$, representing a filled $0s$ shell with eight nucleons occupying the $0p$ shell.

As seen in Table 5, the RGM and NCSM results both suggest significant clustering in the lowest 0^+ , 2^+ , and 4^+ states. While the NCSM is not ideally suited to describe

J^π	$E_{\text{ex}}^{(\text{exp})}$	$E_{\text{ex}}^{(\text{NCSM})}$	$E_{\text{ex}}^{(\text{RGM})}$	S_ℓ
0^+	0	0	0	0.42
2^+	4.4	6.06	3.61	0.49
4^+	14.1	19.8	13.6	0.60

Table 5 Excitation energies (in MeV) for rotational band members in ^{12}C : experimental data, NCSM results, and RGM results (both with $\hbar\omega = 25$ MeV), along with spectroscopic factors S_ℓ for triple-alpha decay.

the Hoyle state, the triple-alpha spectroscopic factor $S(0_2^+) = 0.257$ is reasonable. Furthermore, the squared overlap of the triple-alpha channel ($J^\pi = 0^+$) with a two-fragment channel consisting of the ^8Be ground state ($N_{\text{max}} = 4$) and an α in relative motion with $n = 2$, $\ell = 0$, is 0.51. This large overlap supports the dominance of the sequential decay mechanism through ^8Be .

3.3.6 Scattering problem

Having established a cluster-based framework for spectroscopy of bound and weakly bound states, we now illustrate its extension to scattering. In particular, $\alpha + \alpha$ scattering serves as an instructive example for studying resonances and continuum dynamics in light nuclei.

Unlike the case of deeply bound states, the HO expansion is a poor choice for weakly bound and scattering states because of spatially extended nature of the wave functions. However, the analytic form of the basis functions remedies this issue. The J-matrix method, Ref. [138], also known as the Harmonic Oscillator Representation of Scattering Equations (HORSE) [139, 140], has been extensively discussed in the literature [138]. In its traditional form, which we discuss here, the method is limited to the case where remotely the Hamiltonian matrix is represented just by the kinetic energy operator. The Coulomb problem presents a significant challenge for the standard J-matrix/HORSE method, but the method can be appropriately modified, as discussed in Refs. [106, 139, 140].

The integer n in Eq. (59), which enumerates the basis states, coincides with the number of nodes in the radial part of the wave function. The method relies on the asymptotic limit $r \rightarrow \infty$ in coordinate space being equivalent to the configuration-space limit $n \rightarrow \infty$, with the approximate correspondence

$$r = \sqrt{\frac{\hbar}{m\omega}(2n + \ell + 3/2)}. \quad (61)$$

Thus, the RGM solution (50), expressed in radial form (59) needs to be matched with the asymptotic solution for the free-space Hamiltonian, such that the asymptotic behavior is expressed as

$$\chi_n \simeq \alpha F_{n\ell} + \beta G_{n\ell}, \quad (62)$$

where F_{nl} and G_{nl} represent the regular and irregular solutions for the free-space Hamiltonian (which are Coulomb or Bessel functions), expanded in the HO basis; see Ref. [141].

The central idea, describing the J-matrix (or HORSE) method [138–140], is represented by the following equation, showing the structure of the RGM matrix:

$$\begin{pmatrix} \mathcal{H}_{00} & \cdots & \mathcal{H}_{0n} & 0 & \cdots & 0 \\ \vdots & \ddots & \vdots & 0 & 0 & \vdots \\ \mathcal{H}_{n0} & \cdots & \mathcal{H}_{nn} & T_{nn+1} & 0 & 0 \\ \hline 0 & 0 & T_{n+1n} & T_{n+1n+1} & T_{\dots} & 0 \\ \vdots & 0 & 0 & T_{\dots} & T_{\dots} & \ddots \\ 0 & \cdots & 0 & 0 & \ddots & \ddots \end{pmatrix} \begin{pmatrix} \chi_0 \\ \vdots \\ \chi_n \\ \chi_{n+1} \\ \chi_{n+2} \\ \vdots \end{pmatrix} = E \begin{pmatrix} \mathcal{N}_{00} & \cdots & \mathcal{N}_{0n} & 0 & \cdots & 0 \\ \vdots & \ddots & \vdots & 0 & 0 & \vdots \\ \mathcal{N}_{n0} & \cdots & \mathcal{N}_{nn} & 0 & 0 & 0 \\ \hline 0 & 0 & 0 & 1 & 0 & \vdots \\ \vdots & 0 & 0 & 0 & 1 & 0 \\ 0 & \cdots & 0 & \cdots & 0 & \ddots \end{pmatrix} \begin{pmatrix} \chi_0 \\ \vdots \\ \chi_n \\ \chi_{n+1} \\ \chi_{n+2} \\ \vdots \end{pmatrix} \quad (63)$$

At the core of the method is an approximation that assumes the Hamiltonian and norm kernels in Eq. (51) are range-limited in configuration space up to some maximum value n , related to the radial distance r as described in Eq. (61). The upper-left blocks in (63), spanning from 0 to n nodes, is computed exactly, let us call this space \mathcal{P} and denote matrices and vectors restricted to this subspace with superscript \mathcal{P} . Beyond this point, an asymptotic form is assumed: the norm kernel becomes the identity matrix, and the Hamiltonian kernel is given by the kinetic energy operator, represented by the lower-right blocks on both sides of equation (63). The solution, starting from ξ_n , is matched to the asymptotic form given in Eq. (62).

Here, E denotes the continuous scattering energy. In the asymptotic region, the kinetic energy Hamiltonian in the harmonic oscillator basis is represented by a tridiagonal matrix. Consequently, only a single matrix element, $T_{n\ n+1}$, connects the two blocks (or spaces).

$$\sum_{m=0}^{m=n} (E\mathcal{N}_{nm} - \mathcal{H}_{nm}) \chi_m = T_{n\ n+1} \chi_{n+1}, \quad (64)$$

Relating ξ_n and ξ_{n+1} and writing them both in the asymptotic form, we obtain

$$\alpha F_{n\ell} + \beta G_{n\ell} = \left(\frac{1}{E\mathcal{N}^{(\mathcal{P})} - \mathcal{H}^{(\mathcal{P})}} \right)_{nn} T_{n\ n+1} (\alpha F_{n+1\ell} + \beta G_{n+1\ell}), \quad (65)$$

where the first term on the right is the n th diagonal element of the inverse matrix. This relation allows one to determine the ratio β/α , which in turn determines the scattering phase shift at energy E .

Figure 19 shows the $\ell = 2$ (D -wave) phase shifts for $\alpha + \alpha$ scattering. The solid line corresponds to the phase shift obtained using this method with HO truncation up to $N = 12$ quanta. Once the threshold is adjusted to the experimental Q value, the agreement with data [142] is quite good.

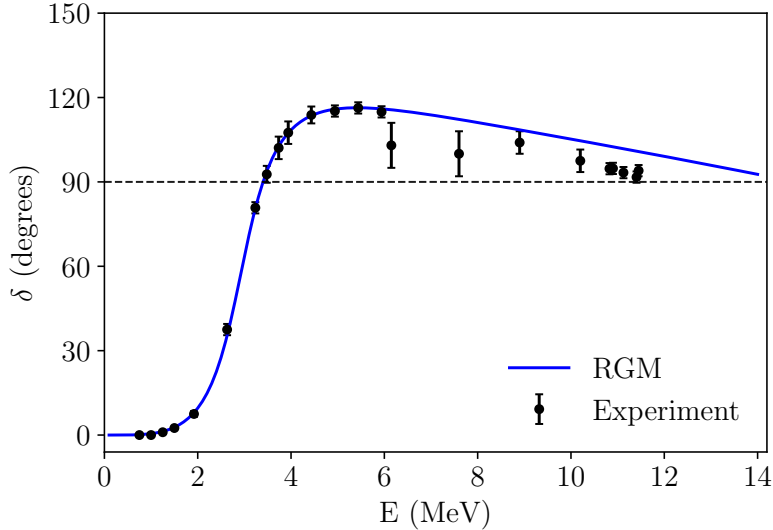


Fig. 19 (Color online) Phase shifts for $\alpha + \alpha$ scattering in the $\ell = 2$ channel. Experimental data are from Ref. [142], while the line shows RGM theoretical results, for further details see Ref. [110]

4 Cluster-shell competition and its modeling

One of the most intriguing features of nuclear structure physics is the interplay between shell and cluster structures [143]. This is mainly caused by the effect of the spin-orbit interaction, which strengthens the symmetry of the jj -coupling shell model. This interaction is well known to be vital in explaining the observed magic numbers of 28, 50, 82 and 126. The spin-orbit interaction also breaks clusters, where some of the strongly correlated nucleons are spatially localised.

Nevertheless, as we discussed in this article, the α cluster structure is important in the light mass region. Be isotopes are known to have a robust α - α cluster structure: ${}^8\text{Be}$ decays into two alpha clusters, and the molecular orbital structure of valence neutrons appears in neutron-rich Be isotopes [144, 145], which has been confirmed by the ab initio calculation as we have seen. The persistence of the α - α cluster structure is due to the alpha-alpha distance, which is about 3–4 fm and large compared to the range of the spin-orbit interaction.

In light nuclei, it is considered that these two different models (shell and cluster) coexist and compete with each other. Although the α - α cluster structure persists in ${}^8\text{Be}$, when one more α cluster is added in ${}^{12}\text{C}$ the interaction among α clusters becomes stronger and the system has a shorter α - α distance. In this case, the alpha clusters are trapped within the interaction range of the spin-orbit interaction. In ${}^{12}\text{C}$, although the three α cluster structure remains in the ground state, the jj -coupling shell model components mix in.

We can model this transition from the cluster state to the shell state owing to the spin-orbit interaction with clear perspective. The α clusters are spin-zero systems, so the spin-orbit interaction — a rank-one non-central interaction — does not contribute

for the systems consisting of the α clusters only. However, we have developed the antisymmetrized quasi cluster model (AQCM) [146–148]. This method enables us to smoothly transform the wave functions of the α -cluster model to those of the jj -coupling shell model. We refer to the clusters that experience the effects of the spin-orbit interaction due to this model as quasi-clusters, which allows us to discuss the intermediate state between this transition from the cluster state to the shell state. We previously introduced AQCM to ^{12}C and discussed the competition between cluster states and the jj -coupling shell model state.

Here, we summarize the basic concept of AQCM, which allows the smooth transformation of cluster model wave functions to jj -coupling shell model ones. In AQCM, as in many other cluster models including the Brink model, each single particle is described by a Gaussian form.

$$\phi^{\tau,\sigma}(\mathbf{r}) = \left(\frac{2\nu}{\pi}\right)^{\frac{3}{4}} \exp\left[-\nu(\mathbf{r}-\zeta)^2\right] \chi^{\tau,\sigma}, \quad (66)$$

where the Gaussian center parameter ζ is related to the expectation value of the position of the nucleon, and $\chi^{\tau,\sigma}$ is the spin-isospin part of the wave function. The Slater determinant is constructed from these single-particle wave functions by antisymmetrizing them. For the Gaussian center parameters $\{\zeta_i\}$, there four single-particle wave functions with different spin and isospin sharing a common ζ value correspond to an α cluster. This cluster wave function is transformed into jj -coupling shell model based on the AQCM. When the original value of the Gaussian center parameter ζ is \mathbf{R} , which is real and related to the spatial position of this nucleon, it is transformed by adding the imaginary part as

$$\zeta = \mathbf{R} + i\Lambda \mathbf{e}^{\text{spin}} \times \mathbf{R}, \quad (67)$$

where \mathbf{e}^{spin} is a unit vector for the intrinsic-spin orientation of this nucleon. The control parameter, labelled as Λ , is associated with the breaking of the α cluster. With a finite value of Λ , the two nucleons with opposite spin orientations have complex conjugate ζ values. This situation corresponds to the time-reversal motion of the two nucleons.

Here, we explain the intuitive meaning of this procedure. Including the imaginary part allows us to connect the single-particle wave function directly to the spherical harmonics of the jj -coupling shell model. Suppose the Gaussian center parameter, represented by the vector symbolized as ζ has an x -component and the spin direction is defined along the z -axis (i.e., a spin-up nucleon). According to Eq. (67), the imaginary part of the x component of the Gaussian center parameter is given to the y component. When we expand $-\nu(\mathbf{r}-\zeta)^2$ in the exponent of Eq. (66), a factor corresponding to the cross term of this expansion appears: $\exp[2\nu\zeta \cdot \mathbf{r}]$. The factor $\exp[2\nu\zeta \cdot \mathbf{r}]$ contains all the information related to the angular momentum of this single particle. The Taylor expansion allows us to show that the p wave component of $\exp[2\nu\zeta \cdot \mathbf{r}]$ is $2\nu\zeta \cdot \mathbf{r}$, which is proportional to $(x + i\Lambda y)$. At the limit of $\Lambda = 1$, this is proportional to Y_{11} of the spherical harmonics. The nucleon is introduced as spin-up, and thus the coupling with the spin part gives the stretched state of the angular momentum, $|3/2 \ 3/2\rangle$ of the

jj -coupling shell model, where the spin-orbit interaction acts attractively. For the spin-down nucleon, we introduce the complex conjugate ζ value, which gives $|3/2 - 3/2\rangle$.

This transformation is quite general, and we can easily generate the jj -coupling shell model wave functions corresponding to the magic numbers 28, 50, and 82 starting with the cluster wave functions. In the case of ^{12}C , we prepare three quasi clusters. The next two nucleons are generated by rotating the ζ values and spin-directions of these two nucleons by $2\pi/3$. The last two nucleons are generated by changing the rotation angle to $4\pi/3$. Eventually, all the six nucleons have spin-stretched states, and after the antisymmetrization, the configuration becomes the subclosure configuration of $(s1/2)^2(p3/2)^4$. This procedure is applied for both proton and neutron parts.

We start the discussion with ^8Be . Our Hamiltonian gives the energy of -27.57 MeV for the α cluster, and thus, -55.1 MeV is the two- α threshold energy (experimentally -56.6 MeV, to which our theoretical value does not contradict). Figure 20 shows the energy curves of the 0^+ state of ^8Be as a function of the distance between two ^4He clusters. The solid line is for $\lambda = 0$ (pure two α 's), and the dotted and dashed line are for two quasi-clusters with $\Lambda = 0.1$ and 0.2 , respectively. The energy minimum point appears around the relative distance of ~ 3.5 fm. This distance is quite large, and this is outside of the interaction range of the spin-orbit interaction. Therefore, the λ value that gives the minimum energy is zero (solid line), which means that the α clusters are not broken. The α breaking effect can be seen in more inner regions, where the energies of dotted and dashed lines are lower than the solid line. The α clusters are surely broken there. However, at short relative distances, the energy itself is high enough, and the spin-orbit interaction only plays a role in reducing the increase of the excitation energy to some extent when two clusters get closer.

Next we discuss ^{12}C . The three- α threshold energy is -82.7 MeV in our calculation compared with the experimental value of -84.9 MeV. Figure 21 shows the energy curves of 0^+ state of ^{12}He with an equilateral triangular configuration as a function of the distance between two ^4He clusters. The solid line is for $\Lambda = 0$ (pure three α 's). Since one ^4He is added to ^8He , the energy minimum point appears around the relative distance of 2.5 – 3.0 fm, shorter by 1 fm than the previous ^8He case before allowing the breaking of α clusters. Therefore, it is considered that the three α clusters step in the interaction range of the spin-orbit interaction. The dotted line ($\Lambda = 0.1$) and dashed line ($\Lambda = 0.2$) almost degenerate at the region of the lowest energy (the relative cluster-cluster distance shrinks to 2 fm there).

It can be summarized that the cluster breaking effect is negligibly small in ^8Be , where α - α cluster structure keeps enough distance; they stay out of the interaction range of the spin-orbit interaction, which breaks the α clusters. The situation is completely different in the ^{12}C case since the additional α cluster shrinks the cluster-cluster distance, and clusters are in the interaction range of the spin-orbit interaction. The ground state of ^{12}C contains the component of the jj -coupling shell model.

Acknowledgments

Regarding the work presented in Sect. 2, TO acknowledges Drs. T. Yoshida, T. Abe, Y. Tsunoda, N. Shimizu, N. Itagaki, Y. Utsuno, H. Ueno, J. Vary and P. Maris for very fruitful collaborative works shown primarily in Refs. [9, 10]. TO thanks Dr. M.

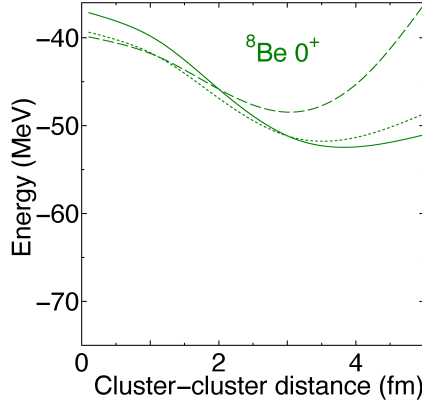


Fig. 20 (a): Energy curves of 0^+ state of ${}^8\text{Be}$ as a function of the distance between two ${}^4\text{He}$ clusters. Solid line is for $\Lambda = 0$ (pure two α 's) and dotted and dashed lines are for two quasi-clusters with $\Lambda = 0.1$ and 0.2 , respectively. See the details in Ref. [149].

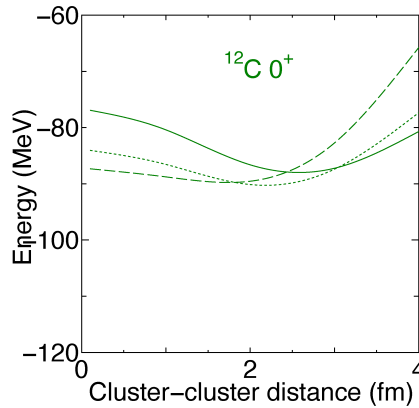


Fig. 21 Energy curves of 0^+ state of ${}^{12}\text{C}$ as a function of the distance between three ${}^4\text{He}$ clusters with equilateral triangular configuration. Solid line is for $\Lambda = 0$ (pure three α 's) and dotted and dashed lines are for two quasi-clusters with $\Lambda = 0.1$ and 0.2 , respectively. See the details in Ref. [149].

Kimura for useful discussions on the clustering, Dr. S. Kuma and Dr. T. Azuma for various information about atomic molecules, and Dr. Y. Aritomo for updating on nuclear fission studies. TO is grateful to Dr. T. Kobori for encouragements crucially contributing to this work. TO and AV acknowledge the visitor program of GANIL, and TO thanks the Alexander von Humboldt Foundation for the Research Award, as some parts of their works were made under these supports. The MCSM (incl. QVSM) calculations quoted in this work were performed on the supercomputers K and Fugaku at RIKEN AICS K and Fugaku at RIKEN AICS (hp190160, hp200130, hp210165, hp220174, hp230207, hp240213, hp250224). The work presented in Sect. 2 are supported in part by JSPS KAKENHI Grant Number JP19H05145 and JP21H00117 as well as JP25K00998. It was also supported in part by MEXT as ‘‘Program for Promoting Researches on the Supercomputer Fugaku’’ (Simulation for basic science: from

fundamental laws of particles to creation of nuclei, JPMXP1020200105, Simulation for basic science: approaching the new quantum era, JPMXP1020230411), and by JICFuS. Regarding the work presented in Sect. 3, AV acknowledges partial support by the US Department of Energy (DOE), Office of Science, Office of Nuclear Physics grant DE-SC0009883. Regarding the work presented in Sect. 4, NI acknowledges partial support by JSPS KAKENHI Grant Numbers JP22K03618 and JP25K01005.

References

- [1] W. V. Wefelmeier, *Z. Phys. Hadrons Nucl.* **107**, 332 (1937).
- [2] W. J. A., *Phys. Rev.* **52**, 1083 (1937).
- [3] H. Morinaga, *Phys. Rev. C* **101**, 254 (1956).
- [4] D. Brink, in *The Proc. Intl. School of Physics Enrico Fermi, Course 36* (247) p. 020030.
- [5] K. Ikeda, N. Takigawa, and H. Horiuchi, *Prog. Thoer. Phys. Suppl.* **E68**, 464 (1968).
- [6] A. Arima, H. Horiuchi, K. Kubodera, and N. Takigawa (Springer, Berlin, Heidelberg, 1973) p. 345.
- [7] M. Freer, H. Horiuchi, Y. Kanada-En'yo, D. Lee, and U.-G. Meißner, *Rev. Mod. Phys.* **90**, 35004 (2018).
- [8] T. Nakamura, K. Shigaki, H. Ohnishi, *et al.*, *Eur. Phys. J. A* **61**, 273 (2025).
- [9] T. Otsuka, Y. Tsunoda, N. Shimizu, Y. Utsuno, T. Abe, and H. Ueno, *Eur. Phys. J. A* **61**, 126 (2025).
- [10] T. Otsuka, T. Abe, T. Yoshida, Y. Tsunoda, N. Shimizu, N. Itagaki, Y. Utsuno, J. Vary, P. Maris, and H. Ueno, *Nat. Commun.* **13**, 2234 (2022).
- [11] E. Uegaki, S. Okabe, Y. Abe, and H. Tanaka, *Prog. Thoer. Phys.* **57**, 1262 (1977).
- [12] M. Kamimura, *Nucl. Phys. A* **351**, 456 (1981).
- [13] A. Tohsaki, H. Horiuchi, P. Schuck, and G. Röpke, *Phys. Rev. Lett.* **87**, 192501 (2001).
- [14] R. Bijker and F. Iachello, *Ann. Phys.* **298**, 334 (2002).
- [15] N. Itagaki, S. Aoyama, S. Okabe, and K. Ikeda, *Phys. Rev. C* **70**, 054307 (2004).
- [16] M. Chernykh, H. Feldmeier, T. Neff, P. Von Neumann-Cosel, and A. Richter, *Phys. Rev. Lett.* **98**, 032501 (2007).
- [17] Y. Kanada-En'yo, *Prog. Thoer. Phys.* **117**, 655 (2007).
- [18] P. Maris, M. A. Caprio, and J. P. Vary, *Phys. Rev. C* **91**, 014310 (2015).
- [19] P. W. Zhao, N. Itagaki, and J. Meng, *Phys. Rev. Lett.* **115**, 022501 (2015).
- [20] A. C. Dreyfuss, K. D. Launey, T. Dytrych, J. P. Draayer, R. B. Baker, C. M. Deibel, and C. Bahri, *Phys. Rev. C* **95**, 044312 (2017).
- [21] R. B. Wiringa, S. C. Pieper, J. Carlson, and V. R. Pandharipande, *Phys. Rev. C: Nucl. Phys.* **62**, 14001 (2000).
- [22] J. Carlson, S. Gandolfi, F. Pederiva, S. C. Pieper, R. Schiavilla, K. E. Schmidt, and R. B. Wiringa, *Rev. Mod. Phys.* **87**, 1067 (2015).
- [23] E. Epelbaum, H. Krebs, T. A. Lähde, D. Lee, and U.-G. Meißner, *Phys. Rev. Lett.* **109**, 252501 (2012).

- [24] A. D’Alessio, T. Mongelli, M. Arnold, S. Bassauer, J. Birkhan, I. Brandherm, M. Hilcker, T. Hüther, J. Isaak, L. Jürgensen, T. Klaus, M. Mathy, P. von Neumann-Cosel, N. Pietralla, V. Yu. Ponomarev, P. C. Ries, R. Roth, M. Singer, G. Steinhilber, K. Vobig, and W. V., *Phys. Rev. C* **102**, 011302 (R) (2020).
- [25] S. Shen, S. Elhatisari, T. Lähde, *et al.*, *Nat. Commun.* **14**, 2777 (2023).
- [26] F. Hoyle, *Astrophys. J. Suppl.* **1**, 121 (1954).
- [27] D. N. F. Dunbar, R. E. Pixley, W. A. Wenzel, and W. Whaling, *Phys. Rev.* **92**, 649 (1953).
- [28] M. Freer and H. O. U. Fynbo, *Prog. Part. Nucl. Phys.* **78**, 1 (2014).
- [29] H. O. U. Fynbo *et al.*, *Nature* **433**, 136–139 (2005).
- [30] S. Jin, L. F. Roberts, S. M. Austin, and H. Schatz, *Nature* **588**, 57 (2020).
- [31] A. M. Shirokov, I. J. Shin, Y. Kim, M. Sosonkina, M. P., and J. P. Vary, *Phys. Lett. B* **761**, 87 (2016).
- [32] A. M. Shirokov, J. P. Vary, A. I. Mazur, and T. A. Weber, *Phys. Lett. B* **644**, 33 (2007).
- [33] National nuclear data center’s “evaluated nuclear structure data file”, <http://www.nndc.bnl.gov/ensdf/> (2026).
- [34] M. Honma, T. Mizusaki, and T. Otsuka, *Phys. Rev. Lett.* **75**, 1284 (1995).
- [35] T. Otsuka, T. Mizusaki, and M. Honma, *Phys. Rev. Lett.* **81**, 1588 (1998).
- [36] T. Otsuka, M. Honma, T. Mizusaki, N. Shimizu, and Y. Utsuno, *Prog. Part. Nucl. Phys.* **47**, 319 (2001).
- [37] N. Shimizu *et al.*, *Prog. Theor. Exp. Phys.* **2012**, 01A205 (2012).
- [38] T. *at al.* Abe, *Phys. Rev. C* **86**, 054301 (2012).
- [39] T. Abe *et al.*, *Phys. Rev. C* **104**, 054315 (2021).
- [40] T. Hastie, R. Tibshirani, and J. Friedman, *The Elements of Statistical Learning: Data Mining, Inference, and Prediction, Second Edition* (Springer, Berlin, 2009).
- [41] G. C. Strinati, P. Pieri, G. Röpke, P. Schuck, and M. Urban, *Phys. Rept.* **738**, 1 (2018).
- [42] A. Bohr, *Mat. Fys. Medd. Dan. Vid. Selsk.* **26**, 14 (1952).
- [43] A. Bohr and B. R. Mottelson, *Mat. Fys. Medd. Dan. Vid. Selsk.* **27**, 16 (1953).
- [44] A. N. Bohr, in *Nobel Lectures, Physics 1971–1980*, edited by S. Lundqvist (World Scientific, Singapore, 1992) p. 213.
- [45] A. Bohr and B. Mottelson, *Nuclear Structure, Vol. II* (Benjamin, New York, 1975).
- [46] P. Ring and P. Schuck, *The Nuclear Many-Body Problem* (Springer, Berlin, 1980).
- [47] S. Johansson, in *Nobel Lectures, Physics 1971–1980*, edited by S. Lundqvist (World Scientific, Singapore, 1992).
- [48] T. Otsuka, arXiv , 2509.08552v2 [nucl (2025)].
- [49] M. Chernykh, H. Feldmeier, T. Neff, P. von Neumann-Cosel, and A. Richter, *Phys. Rev. Lett.* **98**, 032501 (2007).
- [50] W. R. Zimmerman, N. E. Destefano, M. Freer, M. Gai, and F. D. Smit, *Phys. Rev. C* **84**, 027304 (2011).
- [51] W. R. Zimmerman, M. W. Ahmed, B. Bromberger, S. C. Stave, A. Breskin, V. Dangendorf, T. Delbar, M. Gai, S. S. Henshaw, J. M. Mueller, C. Sun,

- K. Tittelmeier, H. R. Weller, and Y. K. Wu, *Phys. Rev. Lett.* **110**, 152502 (2013).
- [52] A. Ogloblin *et al.*, EPJ Web of Conferences **66**, 02074 (2014).
- [53] D. J. Mar'in-L'ambarri *et al.*, *Phys. Rev. Lett.* **113**, 012502 (2014).
- [54] Y. Funaki, *Phys. Rev. C* **92**, 021302 (2015).
- [55] P. Marević, J.-P. Ebran, E. Khan, T. Nikšić, and D. Vretenar, *Phys. Rev. C* **99**, 034317 (2019).
- [56] A. Danilov, T. Belyaeva, A. Demyanova, S. Goncharov, and A. Ogloblin, *Phys. Rev. C* **80**, 054603 (2009).
- [57] T. Otsuka and Y. Utsuno, Quantum appearance of tennis racket effect in atomic nuclei and conservation of k quantum number (tentative) (2026).
- [58] P. Atkins, J. de Paula, and J. Keeler, *Physical Chemistry* (Springer, Berlin, 2012).
- [59] J. K. Krappé and K. Pomorski, *Theory of Nuclear Fission* (Springer, Berlin, 2012).
- [60] W. J. N. *et al.*, *Nature* **590**, 566 (2021).
- [61] G. Gamow, *Proc. R. Soc. Lond. A: Math. Phys. Eng. Sci.* **126**, 632 (1930).
- [62] L. R. Hafstad and E. Teller, *Phys. Rev.* **54**, 681 (1938).
- [63] J. Blatt and V. Weisskopf, *Theoretical Nuclear Physics*, Dover Books on Physics (Dover Publications, 2012).
- [64] N. Sandulescu, M. Sambataro, and A. Volya, EPJ Web Conf. **292**, 1003 (2024).
- [65] C. White, A. Volya, D. Mulhall, and V. Zelevinsky, *Phys. Rev. Res.* **5**, 013109 (2023).
- [66] Y. Kanada-En'yo, M. Kimura, and A. Ono, *Prog. Theor. Exp. Phys.* **2012**, 1A202 (2012).
- [67] J. A. Wheeler, *Phys. Rev.* **52**, 1107 (1937).
- [68] K. Wildermuth and E. J. Kanellopoulos, *Rep. Prog. Phys.* **42**, 1719 (1979).
- [69] J. Draayer, *Nucl. Phys. A* **237**, 157 (1975).
- [70] Y. F. Smirnov and Y. M. Tchuvilsky, *Phys. Rev. C* **15**, 84 (1977).
- [71] W. Chung, J. van Hienen, B. Wildenthal, and C. Bennett, *Phys. Lett. B* **79**, 381 (1978).
- [72] N. Anantaraman, C. L. Bennett, J. P. Draayer, H. W. Fulbright, H. E. Gove, and J. Tō ōke, *Phys. Rev. Lett.* **35**, 1131 (1975).
- [73] A. C. Dreyfuss, K. D. Launey, J. E. Escher, G. H. Sargsyan, R. B. Baker, T. Dytrych, and J. P. Draayer, *Phys. Rev. C* **102**, 044608 (2020).
- [74] T. Dytrych, K. D. Launey, J. P. Draayer, D. J. Rowe, J. L. Wood, G. Rosensteel, C. Bahri, D. Langr, and R. B. Baker, *Phys. Rev. Lett.* **124**, 042501 (2020).
- [75] J.-P. Ebran, E. Khan, T. Nikšić, and D. Vretenar, *Nature* **487**, 341 (2012).
- [76] E. Epelbaum, H. Krebs, D. Lee, and U.-G. Meißner, *Phys. Rev. Lett.* **106**, 192501 (2011).
- [77] S. Elhatisari, D. Lee, G. Rupak, E. Epelbaum, H. Krebs, T. A. Lähde, T. Luu, and U.-G. Meißner, *Nature* **528**, 111 (2015).
- [78] P. Schuck, Y. Funaki, H. Horiuchi, G. Röpke, A. Tohsaki, and T. Yamada, *Phys. Scr.* **91**, 123001 (2016).
- [79] A. Tohsaki, H. Horiuchi, P. Schuck, and G. Röpke, *Rev. Mod. Phys.* **89**, 11002 (2017).

- [80] P. Navrátil and S. Quaglioni, *Phys. Rev. Lett.* **108**, 42503 (2012).
- [81] P. Navrátil, S. Quaglioni, G. Hupin, C. Romero-Redondo, and A. Calci, *Phys. Scr.* **91**, 53002 (2016).
- [82] X. Zhang, S. R. Stroberg, P. Navrátil, C. Gwak, J. A. Melendez, R. J. Furnstahl, and J. D. Holt, *Phys. Rev. Lett.* **125**, 112503 (2020).
- [83] C. W. Johnson, K. D. Launey, N. Auerbach, S. Bacca, B. R. Barrett, C. R. Brune, M. A. Caprio, P. Descouvemont, W. H. Dickhoff, C. Elster, P. J. Fasano, K. Fossez, H. Hergert, M. Hjorth-Jensen, L. Hlophe, B. Hu, R. M. Id Betan, A. Idini, S. König, K. Kravvaris, D. Lee, J. Lei, A. Mercenne, R. N. Perez, W. Nazarewicz, F. M. Nunes, M. Płoszajczak, J. Rotureau, G. Rupak, A. M. Shirokov, I. Thompson, J. P. Vary, A. Volya, F. Xu, R. G. T. Zegers, V. Zelevinsky, and X. Zhang, *J. Phys. G: Nucl. Part. Phys.* **47**, 123001 (2020).
- [84] J. Okołowicz, M. Płoszajczak, and W. Nazarewicz, *Phys. Rev. Lett.* **124**, 042502 (2020).
- [85] A. Volya, *EPL* **130**, 12001 (2020).
- [86] M. L. Avila, G. V. Rogachev, V. Z. Goldberg, E. D. Johnson, K. W. Kemper, Y. M. Tchuvil'sky, and A. S. Volya, *Phys. Rev. C* **90**, 024327 (2014).
- [87] A. N. Kuchera, *Clustering Phenomena in the $A=10$ $T=1$ Isobaric Multiplet*, Ph.D. thesis, unknown (2013).
- [88] J. Okołowicz, M. Płoszajczak, and I. Rotter, *Phys. Rep.* **374**, 271 (2003).
- [89] N. Auerbach and V. Zelevinsky, *Rep. Prog. Phys.* **74**, 106301 (2011).
- [90] K. Kravvaris and A. Volya, *J. Phys.: Conf. Ser.* **863**, 012016 (2017).
- [91] A. Volya, M. Barbui, V. Z. Goldberg, and G. V. Rogachev, *Commun Phys* **5**, 1 (2022).
- [92] E. Koshchiy, G. V. Rogachev, E. Pollacco, S. Ahn, E. Uberseder, J. Hooker, J. Bishop, E. Aboud, M. Barbui, V. Z. Goldberg, C. Hunt, H. Jayatissa, C. Magana, R. O'Dwyer, B. T. Roeder, A. Saastamoinen, and S. Upadhyayula, *Nuclear Instruments and Methods in Physics Research Section A: Accelerators, Spectrometers, Detectors and Associated Equipment* **957**, 163398 (2020).
- [93] M. Barbui, A. Volya, E. Aboud, S. Ahn, J. Bishop, V. Z. Goldberg, J. Hooker, C. H. Hunt, H. Jayatissa, Tz. Kokalova, E. Koshchiy, S. Pirrie, E. Pollacco, B. T. Roeder, A. Saastamoinen, S. Upadhyayula, C. Wheldon, and G. V. Rogachev, *Phys. Rev. C* **106**, 054310 (2022).
- [94] V. Z. Goldberg, A. K. Nurmukhanbetova, A. Volya, D. K. Nauruzbayev, G. E. Serikbayeva, and G. V. Rogachev, *Phys. Rev. C* **105**, 014615 (2022).
- [95] D. K. Nauruzbayev, V. Z. Goldberg, A. K. Nurmukhanbetova, M. S. Golovkov, A. Volya, G. V. Rogachev, and R. E. Tribble, *Phys. Rev. C* **96**, 014322 (2017).
- [96] A. K. Nurmukhanbetova, V. Z. Goldberg, D. K. Nauruzbayev, M. S. Golovkov, and A. Volya, *Phys. Rev. C* **100**, 062802 (2019).
- [97] A. K. Nurmukhanbetova, V. Z. Goldberg, A. Volya, D. K. Nauruzbayev, and G. V. Rogachev, *Eur. Phys. J. A.* **60**, 217 (2024).
- [98] A. K. Nurmukhanbetova, V. Z. Goldberg, A. Volya, D. K. Nauruzbayev, G. E. Serikbayeva, and G. V. Rogachev, *Phys. Rev. C* **109**, 24607 (2024).
- [99] S. Upadhyayula, G. V. Rogachev, J. Bishop, V. Z. Goldberg, J. Hooker, C. Hunt, H. Jayatissa, E. Koshchiy, E. Uberseder, A. Volya, B. T. Roeder, and

- A. Saastamoinen, [Phys. Rev. C **101**, 034604 \(2020\)](#).
- [100] A. Volya, V. Z. Goldberg, A. K. Nurmukhanbetova, D. K. Nauruzbayev, and G. V. Rogachev, [Phys. Rev. C **105**, 014614 \(2022\)](#).
- [101] A. de-Shalit and I. Talmi, *Nuclear Shell Theory*, Dover Books on Physics (Dover, 2004).
- [102] B. R. Barrett, P. Navrátil, and J. P. Vary, [Prog. Part. Nucl. Phys. **69**, 131 \(2013\)](#).
- [103] F. Palumbo and D. Prosperi, [Nucl. Phys. A **115**, 296 \(1968\)](#).
- [104] D. Gloeckner and R. Lawson, [Phys. Lett. B **53**, 313 \(1974\)](#).
- [105] M. Moshinsky and Y. F. Smirnov, *The Harmonic Oscillator in Modern Physics*, Contemporary Concepts in Physics, Vol. 9 (Harwood academic publishers GmbH, Amsterdam, The Netherlands, 1996).
- [106] K. Kravvaris, *Clustering in Light Nuclei with Configuration Interaction Approaches*, Ph.D. thesis, ProQuest Dissertations & Theses (2018).
- [107] A. Volya and Y. M. Tchuvil'sky, [Phys. Rev. C **91**, 044319 \(2015\)](#).
- [108] M. Ichimura, A. Arima, E. C. Halbert, and T. Terasawa, [Nucl. Phys. Sect. A **A204**, 225 \(1973\)](#).
- [109] P. Maris and J. P. Vary, [Int. J. Mod. Phys. E **22**, 1330016 \(2013\)](#).
- [110] K. Kravvaris and A. Volya, [Phys. Rev. C **100**, 034321 \(2019\)](#).
- [111] L. Trlifaj, [Phys. Rev. C: Nucl. Phys. **5**, 1534 \(1972\)](#).
- [112] S. Quaglioni and P. Navratil, [Phys. Rev. C **79**, 044606 \(2009\)](#).
- [113] B. A. Brown, [Physics **4**, 525 \(2022\)](#).
- [114] A. Nurmukhanbetova, V. Goldberg, D. Nauruzbayev, A. Volya, and T. Zholdybayev, [Acta Phys. Pol. B Proc. Suppl. **16**, 1 \(2023\)](#).
- [115] G. F. Filippov, Yu. A. Lashko, S. V. Korennov, and K. Katō, [Few-Body-Systems **33**, 173 \(2003\)](#).
- [116] G. Filippov and Y. Lashko, [Phys. Rev. C **70**, 064001 \(2004\)](#).
- [117] Yu. A. Lashko and G. F. Filippov, [Phys. Atom. Nuclei **71**, 209 \(2008\)](#).
- [118] Yu. A. Lashko, V. S. Vasilevsky, and G. F. Filippov, [Annals of Physics **409**, 167930 \(2019\)](#).
- [119] T. Fliessbach and H. Mang, [Nucl. Phys. A **263**, 75 \(1976\)](#).
- [120] T. Fliessbach and P. Manakos, [J. Phys. G: Nucl. Phys. **3**, 643 \(1977\)](#).
- [121] T. Carey, P. Roos, N. Chant, A. Nadasen, and H. L. Chen, [Phys. Rev. C: Nucl. Phys. **23**, 576\(R\) \(1981\)](#).
- [122] B. A. Brown and W. A. Richter, [Phys. Rev. C **74**, 034315 \(2006\)](#).
- [123] M. Freer, [Rep. Prog. Phys. **70**, 2149 \(2007\)](#).
- [124] R. S. Lubna, K. Kravvaris, S. L. Tabor, V. Tripathi, A. Volya, E. Rubino, J. M. Allmond, B. Abromeit, L. T. Baby, and T. C. Hensley, [Phys. Rev. C **100**, 034308 \(2019\)](#).
- [125] R. S. Lubna, K. Kravvaris, S. L. Tabor, V. Tripathi, E. Rubino, and A. Volya, [Phys. Rev. Research **2**, 043342 \(2020\)](#).
- [126] P. Manakos, T. Fliessbach, and H. Walliser, [Phys. Rev. C **27**, 2930 \(1983\)](#).
- [127] N. Anantaraman, J. P. Draayer, H. E. Gove, J. Tō ōke, and H. T. Fortune, [Phys. Rev. C: Nucl. Phys. **18**, 815 \(1978\)](#).
- [128] F. Tanabe, A. Tohsaki, and R. Tamagaki, [Prog. Theor. Phys. **53**, 677 \(1975\)](#).
- [129] Y. Suzuki and K. Hecht, [Nucl. Phys. A **455**, 315 \(1986\)](#).

- [130] R. Lovas, R. Liotta, A. Insolia, K. Varga, and D. Delion, [Physics Reports](#) **294**, 265 (1998).
- [131] K. Varga, R. Lovas, and R. Liotta, [Nuclear Physics A](#) **550**, 421 (1992).
- [132] R. G. Thomas, [Prog. Theor. Phys.](#) **12**, 253 (1954).
- [133] M. Chernykh, H. Feldmeier, T. Neff, P. von Neumann-Cosel, and A. Richter, [Phys. Rev. Lett.](#) **98**, 32501 (2007).
- [134] Ad.R. Raduta, B. Borderie, E. Geraci, N. L. Neindre, P. Napolitani, M. Rivet, R. Alba, F. Amorini, G. Cardella, M. Chatterjee, E. D. Filippo, D. Guinet, P. Lattes, E. L. Guidara, G. Lanzalone, G. Lanzano, I. Lombardo, O. Lopez, C. Maiolino, A. Pagano, S. Pirrone, G. Politi, F. Porto, F. Rizzo, P. Russotto, and J. Wieleczko, [Phys. Lett. B](#) **705**, 65 (2011).
- [135] M. Itoh, S. Ando, T. Aoki, H. Arikawa, S. Ezure, K. Harada, T. Hayamizu, T. Inoue, T. Ishikawa, K. Kato, H. Kawamura, Y. Sakemi, and A. Uchiyama, [Phys. Rev. Lett.](#) **113**, 102501 (2014).
- [136] R. Smith, Tz. Kokalova, C. Wheldon, J. E. Bishop, M. Freer, N. Curtis, and D. J. Parker, [Phys. Rev. Lett.](#) **119**, 132502 (2017).
- [137] D. Dell'Aquila, I. Lombardo, G. Verde, M. Vigilante, L. Acosta, C. Agodi, F. Cappuzzello, D. Carbone, M. Cavallaro, S. Cherubini, A. Cvetinovic, G. D'Agata, L. Francalanza, G. L. Guardo, M. Gulino, I. Indelicato, M. La Cognata, L. Lamia, A. Ordine, R. G. Pizzone, S. M. R. Puglia, G. G. Rapisarda, S. Romano, G. Santagati, R. Spartà, G. Spadaccini, C. Spitaleri, and A. Tumino, [Phys. Rev. Lett.](#) **119**, 132501 (2017).
- [138] A. D. Alhaidari, E. J. Heller, H. A. Yamani, and M. S. Abdelmonem, eds., *The J-matrix Method: Developments and Applications* (Springer, Dordrecht, 2008).
- [139] J. Bang, A. Mazur, A. Shirokov, Yu.F. Smirnov, and S. Zaytsev, [Annals of Physics](#) **280**, 299 (2000).
- [140] A. M. Shirokov, A. I. Mazur, I. A. Mazur, and J. P. Vary, [Phys. Rev. C: Nucl. Phys.](#) **94**, 64320 (2016).
- [141] H. A. Yamani and L. Fishman, [J. Math. Phys.](#) **16**, 410 (1975).
- [142] S. A. Afzal, A. A. Z. Ahmad, and S. Ali, [Rev. Mod. Phys.](#) **41**, 247 (1969).
- [143] N. Itagaki, S. Aoyama, S. Okabe, and K. Ikeda, [Phys. Rev. C](#) **70**, 054307 (2004).
- [144] N. Itagaki and S. Okabe, [Phys. Rev. C](#) **61**, 044306 (2000).
- [145] N. Itagaki, S. Okabe, and K. Ikeda, [Phys. Rev. C](#) **62**, 034301 (2000).
- [146] N. Itagaki, H. Masui, M. Ito, and S. Aoyama, [Phys. Rev. C](#) **71**, 064307 (2005).
- [147] T. Suhara, N. Itagaki, J. Cseh, and M. Płoszajczak, [Phys. Rev. C](#) **87**, 054334 (2013).
- [148] N. Itagaki and T. Naito, [Phys. Rev. C](#) **103**, 044303 (2021).
- [149] N. Itagaki and E. Hiyama, [Phys. Rev. C](#) **107**, 024309 (2023).